Supergene neoformation of Pt-Ir-Fe-Ni alloys: multistage grains explain nugget formation in Ni-laterites

Thomas Aiglsperger[1]. Joaquín A. Proenza[1]. Mercè Font-Bardia[1]. Sandra Baurier-Aymat[1]. Salvador Galí[1]. John F. Lewis[2]. Francisco Longo[3]

1 Departament de Mineralogia, Petrologia i Geologia Aplicada, Universitat de Barcelona (UB), Martí i Franquès s/n, 08028 Barcelona, Spain
2 Department of Earth and Environmental Sciences, George Washington University, Washington, DC 20052, USA
3 Faculty of Engineering, Universidad Católica Tecnológica del Cibao (UCATECI), Ave. Universitaria, esq. Ave. Pedro Rivera, PO Box 401, La Vega, Dominican Republic

Thomas Aiglsperger
thomas.aiglsperger@ub.edu

ABSTRACT:

Ni-laterites from the Dominican Republic host rare but extremely platinum-group element (PGE)-rich chromitites (up to 17.5 ppm) without economic significance. These chromitites occur either included in saprolite (beneath the Mg discontinuity) or as 'floating chromitites' within limonite (above the Mg discontinuity). Both chromitite types have similar iridium-group PGE (IPGE)-enriched chondrite normalized patterns; however, chromitites included in limonite show a pronounced positive Pt anomaly. Investigation of heavy mineral concentrates, obtained via hydroseparation techniques, led to the discovery of multistage PGE grains: (i) Os-Ru-Fe-(Ir) grains of porous appearance are overgrown by (ii) Ni-Fe-Ir and Ir-Fe-Ni-(Pt) phases which are overgrown by (iii) Pt-Ir-Fe-Ni mineral phases. Whereas Ir-dominated overgrowths prevail in chromitites from the saprolite, Pt-dominated overgrowths are observed within floating chromitites. The following formation model for multistage PGE grains is discussed: (i) hypogene platinum-group minerals (PGM) (e.g. laurite) are transformed to secondary PGM by desulphurization during serpentinization; (ii) at the stages of serpentinization and/or at the early stages of lateritization, Ir is mobilized and recrystallizes on porous surfaces of secondary PGM (serving as a natural catalyst) and (iii) at the late stages of lateritization, biogenic mediated neoformation (and accumulation) of Pt-Ir- Fe-Ni nanoparticles occurs. The evidence presented in this work demonstrates that in situ growth of Pt-Ir-Fe-Ni alloy nuggets of isometric symmetry is possible within Nilaterites from the Dominican Republic.

68

69

70

INTRODUCTION

The platinum-group elements (PGE) are a group of precious metals consisting of Os, Ir, Ru, Rh, Pt and Pd. Due to their unique physical and chemical properties, the PGE are essential for a wide range of industrial applications (e.g. electronics, pollution control via catalytic converters); medicine (e.g. cancer treatment) and jewellery. Currently, ~80 % of the global demand of PGE is provided by two major magmatic ore deposits: the Bushveld Complex in the Republic of South Africa and Noril'sk located in the Russian Federation (USGS 2015). Supergene ore deposits of platinum-group minerals (PGM) placers are historically important and include those found in the surroundings of Ural-Alaskan type complexes (Johan 2002). However, the origin of PGE nuggets found in surface environments is still a matter of scientific debate and two opposing genetic models exist: (i) PGM crystallize exclusively under hypogene conditions and are mechanically liberated at the surface by weathering of the source rock (Koen 1964; Cabri and Harris 1975; Hattori and Cabri 1992) and (ii) PGM can also form in situ after PGE mobilization during weathering and accretion within the supergene environments (Augusthitis 1965; Ottemann and Augustithis 1967; Stumpfl 1974; Bowles 1986).

The PGE are not 'noble and inert'. They have long been known to be soluble under appropriate conditions and the formation of organo-metallic complexes with Pt were described by Zeise (1831). More recent experiments have shown that PGE can be mobilized under surface conditions (e.g. Bowles et al. 1994; Varajão et al. 2000; Azaroual et al. 2001; Colombo et al. 2008), but there are only a few descriptions from natural sites showing evidence for PGE mobilization and reprecipitation (e.g. Talovina and Lazarenkov 2001;Melcher et al. 2005; Cabral et al. 2007, 2009; Suárez et al. 2010; Garuti et al. 2012; Oberthür et al. 2003, 2014; Campbell et al. 2015). However, in a recent study, Reith et al. (2016) reported that Pt is mobile under surface conditions and can become bioavailable. The possibility of biogenic PGE cycling with subsequent biomineralization of PGM has opened a new approach to explain supergene PGM occurrences. Botryoidal PGM with strong biophilic element concentrations (i.e. iodine) were found in tropical soils from Brazil and the Dominican Republic (Cabral et al. 2011; Aiglsperger et al. 2015, respectively).

This work reports the discovery of multistage PGE grains found in Ni-laterites and aims to contribute to the ongoing debate on the genesis of PGM found in the supergene environment. Emphasis is given to (i) documenting new insights on lowtemperature PGE mobility, (ii) providing clear textural evidence for in situ PGM neoformation and (iii) discussing the possibility of 'nugget growth' in Ni-laterites.

Sample provenance and methodology

The study area is the ophiolite-related Loma Caribe peridotite located within the central part of the Dominican Republic which currently hosts one of the largest resources of Ni-laterite in the Greater Antilles (Redwood 2014) (Fig. 1). The weathering profile developed from the underlying serpentinized ultramafic rocks (harzburgite > dunite > lherzolite) and consists of a Feoxide(s)-dominated limonitic

108 cover at the top and a thick Mgsilicate saprolite horizon beneath (for details, see Lewis et al. 2006;

109 Tauler et al. 2009; Villanova-de-Benavent et al. 2014; Aiglsperger et al. 2016). Samples were taken in

110 the Falcondo mining area: (i) from the Loma Peguera ore deposit which is characterized by the scarce

111 incorporation of small-scale (approx. 2 m in diameter), PGE-rich (~3 ppm) chromitite bodies in

112 saprolite (Proenza et al. 2007; Aiglsperger et al. 2015) and (ii) from the Loma Larga ore deposit hosting

113 a recently discovered, highly weathered chromitite body included in limonite ('floating chromitite')

114 (Figs. 1 and 2).

115 Whole rock PGE contents were obtained at Genalysis Ltd. (Maddington, Western Australia) by ICP-MS

116 (detection limits: 1 ppb for Rh and 2 ppb for Os, Ir, Ru, Pt and Pd) after nickel sulphide fire assay

117 collection, following the method described by Chan and Finch (2001).

118 A total of 100 g of homogenized limonite-chromitite sample from Loma Larga was processed by means

119 of hydroseparation techniques at the HS laboratory Barcelona (Aiglsperger et al. 2015 and reference

120 therein). The resulting heavy mineral concentrates were mounted as polished monolayer resin blocks

121 and subsequently investigated by reflected light microscopy and by scanning electron microscopy

122 (SEM) using a Quanta 200 FEI XTE 325/D8395 with a tungsten filament as well as a field emission

123 scanning electron microscope (FE-SEM) Jeol JSM-7100 at the Serveis Científics I Tecnòlogics,

124 University of Barcelona, Spain. At the same institution, a selection of PGE grains were further

125 investigated by wavelength-dispersive spectroscopy (WDS) element distribution maps using a JEOL

126 JXA-8230 electron microprobe (EMP) with an accelerating voltage of 20 kV and a beam current of

127 128.8 nA. Maps were collected by beam scanning with dwell times of 60 ms/pixel. For each element,

128 the background map was subtracted from the corresponding peak map. Quantitative EMP analyses were

129 obtained with the same instrument in WDS mode, operating with an accelerating voltage of 20 kV, a

130 beam current of 10 nA and a beam diameter of 1 μm. Pure metals were used as standards for Os, Ir, Ru,

131 Rh, Pt, Pd, Co, Sb and Vas well as chromite (Cr, Al, Fe), periclase (Mg), rhodonite (Mn), rutile (Ti),

132 NiO (Ni) and S (S), CuFeS2 (Cu), GaAs (As) and wollastonite (Si). The following interferences RuLβ

133 → RhLα, IrLα → CuKα, RhLβ → PdLα, RuLβ → PdLα, CuKβ → OsLα and RhLα → PtLα were

134 corrected online. A selection of PGM was investigated by xray diffraction (XRD) analysis at the Serveis

135 Científics i Tecnòlogics (University of Barcelona). The x-ray intensity data were measured on a D8

136 Venture system equipped with a multilayer monochromator and a Mo microfocus (λ = 0.71073 Å) and a

137 two-dimension detector. The sample was analysed at a distance of 34 mm. The angles of the goniometer

138 were 2 theta = 0°, omega = 360° and chi = 90° and the sample was spun 360°. The measuring time was

139 of 60 s per step. Subsequent results were processed with Bruker software (TOPAS), which was used to

140 subtract the background of the patterns, to detect the peaks and to assign mineral phases and their

141 corresponding dhkl to each peak.

142

143 **RESULTS**
144
145 **PGE geochemistry and the observation of multistage PGE grains**
146 Whole rock PGE analyses for the 'floating chromitite' revealed high total PGE concentrations of 17.5
147 g/t (Table 1). Comparison of chondrite normalized patterns with chromitite samples from underlying
148 saprolite shows a similar, characteristic iridium-group PGE (IPGE) (Os, Ir and Ru) enrichment relative
149 to PPGE (Rh, Pt and Pd). However, Ir reveals a slight negative anomaly, Rh shows a much more
150 pronounced negative anomaly and Pt has a clear positive anomaly (Fig. 3). Ratios of Pt/Pd change from
151 51 in the chromitite from the saprolite to 163 in the 'floating chromitite', Pt/Ir from 0.51 to 0.66, Pt/Rh
152 from 2.68 to 8.12, Pt/Ru from 0.29 to 0.35 and Pt/Os from 0.50 to 0.46, respectively (Table 1).
153 Approximately 300 grains of PGMin the size range of <20 to 125 μm were detected and classified into
154 three groups according to their textures and associations:
155 (i) Primary PGM as inclusions in chromite (e.g. unaltered laurite).
156 (ii) Secondary PGM after weathering (e.g. interpreted as having formed due to desulphurization during
157 serpentinization).
158 (iii) PGMwith delicate morphologies different to (i) and (ii), suggestive for neoformation processes (e.g.
159 accumulation of nanoparticles within pores of Fe oxide(s)).
160 The vast majority (>90 %) of detected PGM from the 'floating chromitite' of Loma Larga are complex
161 Ru-Os-rich, Fe - bearing secondary PGMof group (ii) and are investigated separately. However, several
162 grains of PGM show a characteristic zonation due to close spatial relationships of individual PGM,
163 hence suggesting different stages of PGM formation: (a) Os-Ru-Fe-(Ir) grains with a porous appearance
164 and occasional intact crystal shapes are overgrown by (b) finegrained Ni-Fe-Ir and Ir-Fe-Ni-(Pt) phases
165 which are subsequently followed by (c) a layer of rounded shaped Pt-(Ir)-bearing minerals (Fig. 4). It is
166 important to note that Ru-Osrich secondary PGM associated with Ir-dominated PGM have been reported
167 from Loma Peguera previously (e.g. Zaccarini et al. 2009; McDonald et al. 2010). However, complete
168 sequences of multistage PGE grains are only observed within the 'floating chromitite' from Loma
169 Larga.
170 In general, quantitative EMP analyses reveal that Fe and Pt are progressively enriched from interpreted
171 early to late domains within multistage PGE grains (Fig. 5). Relatively high concentrations of Al (2.4
172 wt%), Si (1.4 wt%) and S (0.3 wt%), most likely attributed to the presence of Fe-oxide(s) (Al),
173 secondary silica (Si) and organic material (S), are measured within Pt-(Ir) - bearing mineral phases (Fig.
174 5 and Table 2). Element distribution maps show the described zonation trends of individual PGM;
175 however, micron-sized Ru-rich phases occur also within the Ir-Fe-Ni-(Pt) sequence (Fig. 6). It is worth
176 mentioning that the highest Ni concentrations (∼37 wt%) are observed precisely at the top of the Ru-Os-
177 Fe-(Ir) grain with the porous appearance as seen in Figs. 5 and 6.
178 FE-SEM BSE images from one well-preserved multistage PGE grain point to a close relationship
179 between aqueous solutions and agglutination processes as matrix pores are clearly filled by Pt (+Ir)
180 nanoparticles (Fig. 7). Moreover, element distribution maps of the same grain provide good evidence
181 that Pt-dominated nanoparticles gradually replace the secondary Ru-Os-Fe grain (Fig. 8). Indeed, some
182 multistage PGE grains show only small-scale, irregularly-formed remnants of secondary Ru-Os-Fe
183 grains in their central parts (Fig. 9). Others do not show any visible signs of Ru-Os – bearing PGM and
184 hence are considered entirely replaced by accumulations of Pt-Ir-Fe-Ni nanoparticles (Fig. 10).
185
186 **Composition of supergene Pt-Ir-Fe-Ni nanoparticles**
187 The fact that in situ neoformed Pt-Ir-Fe-Ni grains consist of accumulations of nanoscale particles makes
188 EMP analyses challenging. However, representative results (n = 15) out of 60 analyses (16 grains) show
189 low totals ranging from 82.63 to 95.22 wt% with an average of 90.00 wt% (Table 3). The average
190 composition (and range in composition) (in wt%) of Pt-Ir-Fe-Ni grains is: Pt 12.73 (bdl–23.90), Ir 26.89
191 (11.51–40.12), Fe 24.90 (18.77–30.02), Ni 23.12 (9.52–52.71), S 0.02 (bdl-0.09), As 0.05 (bdl-0.16), Os
192 0.15 (bdl-0.54), Ru 0.46 (0.02–1.81), Rh 0.75 (0.14–1.80), Pd 0.03 (bdl-0.25), Fe 24.90 (18.77–30.02),
193 Cu (n = 6) 0.71 (0.43–1.30), Co 0.23 (0.05–0.72), Si 0.24 (0.06–0.57), Al 0.12 (bdl-0.30), Mg 0.01 (bdl-
194 0.04) and Sb 0.01 (bdl-0.10). The absence of significant amounts of S, As and Sb as well as preliminary
195 Raman spectroscopy analyses (flat signals) suggest that Pt-Ir-Fe-Ni grains are alloys with variable
196 compositions. To assess possible solid solutions, compositions were plotted as atomic proportions in
197 ternary diagrams (Fig. 11). In the Ir-Ni-Fe ternary diagram, a constant Ir and Fe enrichment relative to

Ni is observed (Fig. 11a). Interestingly, our data suggest a linear trend from awaruite (Ni3Fe) towards the Fe-dominated compositional field, previously defined as 'hexaferrum' (e.g. McDonald et al. 2010 and reference therein). However, some data points of the trend plot within the Ni-dominated compositional field of garutiite (McDonald et al. 2010). In the Pt-Ni-Fe ternary, no Pt enrichment is observed for high Ni compositions; hence, data points follow along the Pt baseline from awaruite towards Fe-dominated compositions (Fig. 11b). However, at a composition of approximately 60 at.% Fe, Pt enrichment is observed which supports a late-stage formation of Pt-dominated alloys within the limonite. The (Pt + Ir)-Ni-Fe ternary reveals a preferential composition close to $(Pt, Ir)_{0.3}Ni_{0.25}Fe_{0.45}$ (Fig. 11c). Overall, a general Pt + Ir enrichment with concurrent loss of Ni + Fe is strongly supported by a clear inverse correlation (Fig. 12).

Crystallographic data of supergene Pt-Ir-Fe-Ni alloys

Grain selection

One representative Pt-Ir-Fe-Ni alloy of approximately 50 × 90 μm in diameter was separated from the heavy mineral concentrate and fist investigated as a loose grain without polishing. Under the stereomicroscope, the grain shows a rounded shape and metallic luster (Fig. 13a). A detailed examination of the same grain via FE-SEM revealed that it consists of accumulations of Pt-Ir-Fe-Ni nanoparticles (Fig. 13b, c). EMP analyses gave an average composition of $(Pt, Ir)_{0.28}Ni_{0.27}Fe_{0.45}$ for this grain. Moreover, BSE images of the polished grain show zones of bright and densely packed Pt-Ir-Fe-Ni nanoparticles as well as darker occurring zones with micro- and nanochannels indicative for the growing front (Fig. 13d-f).

Diffraction

The same grain was studied using a single-crystal x-ray diffractometer. The obtained diffraction pattern displayed characteristic concentric, well defined and homogeneous Debye rings, indicating that the grain is constituted by a randomly oriented polycrystalline assemblage (insert in Fig. 14). Integration of the intensity data at constant steps of 2Θ gives a conventional one dimensional powder diffraction pattern (Fig. 14). A careful comparison with literature data for chemically related mineral phases revealed that the supergene Pt-Ir- Fe-Ni alloy has similar x-ray line intensities and observed dspacings as awaruite (Table 4). Neither similarities with hexaferrum nor garutiite were observed in terms of x-ray powder pattern. As a consequence, the neoformed Pt-Ir-Fe-Ni alloy most likely represents a new intermetallic member in the isometric system which crystallizes in the space group Fm3m. On this basis, x-ray powder pattern for the Pt-Ir-Fe-Ni alloy was indexed, leading to the refined unit cell dimensions: a=3.6403 (17) Å,V=48.240 (69) Å3, Z = 4. (Table 5).

DISCUSSION

Genesis of multistage PGE grains

It is widely accepted that primary PGM formed during the magmatic stage can be affected by subsequent weathering processes. For example, serpentinization is believed to lead to desulphurization of primary laurite and erlichmanite, thus causing a transformation into Ru-Os mineral phases with porous appearance which are frequently reported as Bsecondary PGM^ (Stockman and Hlava 1984; González-Jiménez et al. 2014 and references therein). Detailed investigation of several free grains of secondary PGM from the saprolitic horizon of Loma Peguera has shown that some exhibit well-preserved rims ofMg silicates as well as fine-grained intergrowths of nanoscale Ru-Os alloys with Mg silicates (see Fig. 7b–d in Aiglsperger et al. 2015). These observations suggest a close relationship between formation of secondary PGM and serpentinization. However, incorporated Mg silicates are not stable at higher levels in the lateritic profile (above the Mg discontinuity) which leads to weathering of Mg silicates and hence to formation of highly porous secondaryPGM. It is proposed that their surface, characterized by a high specific area, serves as a natural catalyst promoting formation processes. With respect to multistage PGE grains, Ni-, Ir- and Fe - enriched fluids, believed to be mobilized during serpentinization and/or earlier stages of lateritization, have apparently crystallized on such secondary, porous Ru-Os-Fe minerals. Such grain associations were observed by Ahmed and Bevan (1981) who reported on the formation of Ir-rich (up to 10 at.%) awaruite on crystals of Ru-Os-Ir-Fe-Ni alloys during serpentinization. This is in good agreement with our quantitative data which show a clear solid solution trend between awaruite and Ir-rich Pt-Ir-Fe-Ni alloys (Fig. 12). In addition, Zhmodik et al. (2004) performed experiments on the iridium distribution in hydrothermally synthesized sulphides and found that a characteristic enrichment of Ir along the external surface of individual large crystals occurs. These authors concluded that this observation is explained by adsorption equilibrium.

However, multistage PGE grains from the highest levels of the Ni-laterite show an overgrowth of Pt-dominated Pt-Ir-Fe- Ni alloys. This indicates that Pt mobilization and subsequent in situ neoformation occurs within the so-called critical zone, characterized by complex interactions of rock, soil, water, air, plants, organic acids and (micro-)organisms (Chorover et al. 2007). It is suggested that Pt (+Ir) are mobilized in the form of chloride complexes under low pH and high Eh conditions prevailing close to the surface of Ni-laterites (Bowles et al. 1994; Azaroual et al. 2001).

PGE nugget formation in Ni-laterites: from hypogene to supergene

The observed positive Pt anomaly in chondrite normalized patterns in the chromitite from the limonite, absent in the underlying chromitite from the saprolite (Fig. 3), together with the observations of Pt-bearing mineral overgrowths (Fig. 4) and complete replacement of secondary Ru-Os-Fe grains by supergene Pt-Ir-Fe-Ni alloys (Figs. 8, 9 and 10), are strong arguments that Pt-dominated PGE nugget formation in lateritic soils is possible. Laboratory experiments demonstrate bioreductive deposition of Pt nanoparticles on bacteria (e.g. Konishi et al. 2007). Hence, in situ neoformation of Pt-Ir-Fe-Ni alloys observed in the present study is thought to be linked to detoxifying biofilms within a porous matrix of secondary Fe oxide(s). Although conditions and processes favouring biogenic growth of alloys in Ni-laterites are subjects of ongoing research, it can be speculated that enzymes play a key role in PGE biomineralization at the nanoscale (Sharma et al. 2013). Supergene processes have been successfully simulated in a laboratory model for in vitro 'growth' of millimetresized gold grains (Shuster and Southam 2014) which reveal similar textures as unpolished Pt-Ir-Fe-Ni grains of this study (Fig. 10i). However, Brugger et al. (2013) investigated the contrasting behaviour of platinum and gold in surface environments and concluded that Au has a higher cell-toxicity compared to Pt-complexes, resulting in Au-detoxifying biofilms and subsequent formation of spheroidal nanoparticles. Such features were not observed for Pt and can be explained by its lower toxicity. However, Le et al. (2006) assessed bioleaching of weathered saprolite nickel ore by using heavy metal tolerant fungi (Aspergillus foetidus) and observed that the presence of multi-metals (e.g. Ni, Fe, Co, Al, Cr, Cu, Mg, Mn, Zn) led to greater toxic response to the growth behaviour of the microorganism relative to single metals. This could explain a sufficient toxicity for the formation of Pt (+Ir)-detoxifying biofilms in the case of Ni-laterites, promoting in situ Pt-Ir-Fe-Ni alloy neoformation. Our observations also indicate a close spatial relationship between hypogene (Os- and Ru-dominated) and supergene PGM (Pt- and Ir-dominated) (Fig. 8). Continuous precipitation of nano-scaled Pt-Ir-Fe-Ni alloys within and around porous secondary

293   PGM leads to porosity reduction, replacement of host minerals (Fig. 9) and ultimately growing of
294   densely packed, mechanically stable Pt-Ir-Fe-Ni alloys (Fig. 13). It is clear that only these grains, having
295   a cubic symmetry (Table 4), are suitable for subsequent transportation and deposition in e.g. stream
296   sediments.
297   In summary, Fig. 15 shows a simplified model for the proposed formation of multistage PGE grains
298   together with examples of representative PGM at different (trans-)formation stages: (i) formation of
299   primary PGM included in chromian spinel at the magmatic stage; (ii) formation of secondary PGM due
300   to desulphurization of primary PGM during serpentinization (involving Mg silicates); (iii) neoformation
301   of Ir-rich Fe-Ni alloys (awaruite?) on the surface of highly porous secondary PGM during
302   serpentinization and/or at the early stages of lateritization; (iv) continuous neoformation of Pt-Ir-Fe-Ni
303   nanoparticles around (and within) secondary PGM and layers of Ir-rich Fe-Ni alloys, close to the surface
304   at the late stages of lateritization, resulting in in situ growth of densely packed Pt-Ir-Fe-Ni nuggets (Fig.
305   16).
306
307   .

308 **CONCLUSIONS**

309

310 Considering the constantly growing number of experimental laboratory studies confirming that PGE are

311 mobilized and can re-crystallize in low-temperature environments, surprisingly little mineralogical

312 evidence from field sites is currently available. Hence, multistage PGE grains found in the uppermost

313 levels of Ni-laterites are good objects to investigate PGM (trans-) formations from hypogene to

314 supergene environments.

315 In this work, we present evidence suggesting that (i) in situ neoformation of Pt-Ir-Fe-Ni alloys occurs in

316 Ni-laterites and that (ii) accumulation of most likely biogenically mediated Pt-Ir-Fe-Ni nanoparticles can

317 result in nugget formation of cubic symmetry.

318 Whereas strong evidence for solely hypogene nugget formation may exist in other environments, the

319 discovery of multistage PGE grains in Ni-laterites suggest that evidence for hypogene and supergene

320 processes can also occur closely linked to each other.

321

334   **REFERENCES**

335

336   Ahmed Z, Bevan JC (1981) Awaruite, iridian awaruite and a new Ru-Os-Ir-Ni-Fe alloy from the
337   Sakhakot-Qila complex, Malakand agency, Pakistan. Min Mag 44:225–230

338   Aiglsperger T, Proenza JA, Lewis JF, Labrador M, Svojtka M, Rojas-Purón A, Longo F, Ďurišová J
339   (2016) Critical metals (REE, Sc, PGE) in Ni-laterites from Cuba and the Dominican Republic.
340   Ore Geol Rev 73:127–147

341   Aiglsperger T, Proenza JA, Zaccarini F, Lewis JF, Garuti G, Labrador M, Longo F (2015) Platinum
342   group minerals (PGM) in the Falcondo Ni-laterite deposit, Loma Caribe peridotite (Dominican
343   Republic). Mineral Deposita 50:105–123

344   Augusthitis SS (1965) Mineralogical and geochemical studies of the platiniferous dunite–birbirite–
345   pyroxenite complex of Yubdo, Birbir, W. Ethiopia. Chem Erde 24:159–196

346   Azaroual M, Romand B, Freyssinet P, Disnar JR (2001) Solubility of platinum in aqueous solutions at
347   25 °C and pHs 4 to 10 under oxidizing conditions. Geochim Cosmochim Acta 65:4453–4463

348   Begizov VD, Borisenko LF, Uskov ED (1975) Sulphides and natural solid solutions of PGE from
349   ultramafic rocks of the Gusevogorsk massif (the Urals). Dokl Acad Sci USSR, Earth Sci Sect
350   225:134–137

351   Bowin CO (1966) Geology of the Central Dominican Republic (a case history of part of an island arc).
352   In: Hess, H. (Ed.), Caribbean geological studies. Mem Geol Soc Am 98:11–84

353   Bowles JFW (1986) The development of platinum-group minerals in laterites. Econ Geol 81:1278–1285

354   Bowles JFW, Gize AP, Vaughan DJ, Norris SJ (1994) Development of platinum-group minerals in
355   laterites-initial comparison of organic and inorganic controls. Transact Instn Min Metall
356   103:B53–B56

357   Brugger J, Etschmann B, Grosse C, Plumridge C, Kaminski J, Paterson D, Shar SS, Ta C, Howard DL,
358   de Jonge MD, Ball AS, Reith F (2013) Can biological toxicity drive the contrasting behavior of
359   platinum and gold in surface environments? ChemGeol 343:99–110

360   Cabral AR, Beaudoin G, Choquette M, Lehmann B, Polônia JC (2007) Supergene leaching and
361   formation of platinum in alluvium: evidence from Serro, Minas Gerais, Brazil. Miner Petrol
362   90:141–150

363 Cabral AR, Lehmann B, Tupinambá M, Schlosser S, Kwitko-Ribeiro R, De Abreu FR (2009) The
364   platiniferous Au-Pd belt of Minas Gerais, Brazil, and genesis of its botryoidal Pt-Pd aggregates.
365   Econ Geol 104:1265–1276

366 Cabral AR, Radtke M, Munnik F, Lehmann B, Reinholz U, Riesemeier H, Tupinambá M, Kwitko-
367   Ribeiro R (2011) Iodine in alluvial platinum-palladium nuggets: evidence for biogenic precious-
368   metal fixation. Chem Geol 281:152–132

369 Cabri LJ, Harris DC (1975) Zoning in Os-Ir alloys and the relation of the geological and tectonic
370   environment of the source rocks to the bulk Pt: Pt + Ir + Os ratio for placers. Can Mineral
371   13:266–274

372 Campbell SG, Reith F, Etschmann B, Brugger J, Martinez-Criado G, Grodon RA, Southam G (2015)
373   Surface transformations of platinum grains from Fifield, new South Wales, Australia. Am Min
374   100: 1236–1243

375 Chan TK, Finch IJ (2001) Determination of platinum-group elements and gold by inductively coupled
376   plasma mass spectrometry. In: Australian platinum conference. Perth, Western Australia, pp 1–9

377 Chorover J, Kretzschmar R, Garcia-Pichel F, Sparks DL (2007) Soil biogeochemical processes within
378   the critical zone. Elements 3: 321–326

379 Colombo C, Oated CJ, Monhemius AJ, Plant JA (2008) Complexation of platinum, palladium and
380   rhodium with inorganic ligands in the environment. Geochem Explor Environ Anal 8:91–101

381 Escuder-Viruete J, Pérez-Estaún A, Contreras F, Joubert M, Weis D, Ullrich TD, Spadea P (2007)
382   Plume mantle source heterogeneity through time: insights from the Duarte complex, Hispaniola,
383   Northeastern Caribbean. J Geophys Res 112(B04203)

384 Garuti G, Zaccarini F, Proenza JA, Thalhammer OAR, Angeli N (2012) Platinum-group minerals in
385   chromitites of the Niquelândia layered intrusion (central Goias, Brazil): their magmatic origin
386   and lowtemperature reworking during serpentinization and lateritic weathering. Minerals 2:365–
387   384

388 González-Jiménez JM, GriffinWL, Gervilla F, Proenza JA, O'Reilly SY, Pearson NJ (2014) Chromitites
389   in ophiolites: how, where, when, why? Part I. Origin and significance of platinum-group
390   minerals. Lithos 189:127–139

391 Hattori K, Cabri LJ (1992) Origin of platinum-group-mineral nuggets inferred from an osmium-isotope
392   study. Can Mineral 30:289–301

393   Johan Z (2002) Alaskan-type complexes and their platinum-group element mineralization. In: Cabri LJ
394   (ed) The geology, geochemistry, mineralogy and mineral beneficiation of platinum-group
395   elements. Can Inst Min Metall Petrol Spec 54:211–249

396   Koen GM(1964) Rounded platinoid grains in theWitwatersrand Banket. Trans Geol Soc S Afr 67:139–
397   147

398   Konishi Y, Ohno K, Saitoh N, Nomura T, Nagamine S, Hishida H, Takahashi Y, Uruga T (2007)
399   Bioreductive deposition of platinum nanoparticles on the bacterium Shewanella algae. J of
400   Biotech 128: 648–653

401   Le L, Tang J, Ryan D, Valix M (2006) Bioleaching nickel laterite ores using multi-metal tolerant
402   Aspergillus foetidus organism. Min Eng 19:1259–1265

403   Lewis JF, Draper G, Proenza JA, Espaillat J, Jiménez J (2006) Ophioliterelated ultramafic rocks
404   (serpentinites) in the Caribbean region: a review of their occurrence, composition, origin,
405   emplacement and nickel laterite soils. Geol Acta 4:237–263

406   McDonald AM, Proenza JA, Zaccarini Z, Rudashevsky NS, Cabri LJ, Stanley CJ, Rudashevsky VN,
407   Melgarejo JC, Lewis JF, Longo F, Bakker RJ (2010) Garutiite, (Ni,Fe,Ir), a new hexagonal
408   polymorph of native Ni from Loma Peguera, Dominican Republic. Eur J Mineral 22:293–304

409   Melcher F, Oberthur T, Lodziak J (2005) Modification of detrital platinum-group minerals from the
410   eastern Bushveld complex, South Africa. Can Mineral 43:1711–1734

411   Naldrett AJ, Duke JM (1980) Platinum metals in magmatic sulfide ores. Science 208:1417–1428

412   Oberthür T, Weiser TW, Gast L (2003) Geochemistry and mineralogy of platinum-group elements at
413   Hartley platinum mine, Zimbabwe. Part 2: supergene redistribution in the oxidized main sulfide
414   zone of the great dyke, and alluvial platinum-group minerals. Mineral Deposita 38:344–355

415   Oberthür T,Weiser TW, Melcher F (2014) Alluvial and eluvial platinumgroup minerals from the
416   Bushveld complex, South Africa. S Afr J Geol 117:255–274

417   Ottemann J, Augustithis SS (1967) Geochemistry and origin of Bplatinum-nuggets^ in lateritic covers
418   from ultrabasic rocks and birbirites of W. Ethiopia. Mineral Deposita 1:269–277

419   Proenza JA, Zaccarini F, Lewis JF, Longo F, Garuti G (2007) Chromian spinel composition and the
420   platinum group minerals of the PGE-rich Loma Peguera chromitites, LomaCaribe peridotite,
421   Dominican Republic. Can Mineral 45: 631–648

422   Redwood S (2014) Gold surge mining is booming in the Dominican Republic as investors follow the
423   gold rush. Min J 24:23–27

424   Reith F, Zammit CM, Shar SS, Etschmann B, Bottrill R, Southam G, Ta C,Kilburn M, Oberthür T, Ball
425   AS, Brugger J (2016) Biological role in the transformation of platinum-group-mineral grains.
426   Nat Geosci 9:294–298

427   Rudashevsky NS, Mochalov AG, Menshikov YP, Shumskaya NI (1983) Ferronickelplatinum, Pt2FeNi,
428   a new mineral species. Zap Vseross Mineral Obshch 112:487–494 (in Russian)

429   Sharma S, Mandani S, Sarma TK (2013) Biogenic growth of alloys and core-shell nanostructures using
430   urease as a nanoreactor at ambient condition. Sci Rep 3(2601):1–8

431   Shuster J, Southam G (2014) The in-vitro "growth" of gold grains. Geology 43:79–82

432   Stockman HW, Hlava PF (1984) Platinum-group minerals in alpine chromitites from South-Western
433   Oregon. Econ Geol 79:491–508

434   Stumpfl EF (1974) The genesis of platinum deposits. Further thoughts. Min Sci Eng 6:120–141

435   Suárez S, Prichard HM, Velasco F, Fisher PC, McDonald I (2010) Alteration of platinum-group
436   minerals and dispersión of platinum-group elements during progressive weathering of the
437   Aguablanca Ni-Cu deposit, SW Spain. Mineral Deposita 45:331–350

438   Talovina IV, Lazarenkov VG (2001) Distribution and genesis of platinum group minerals in nickel ores
439   of the Sakhara and Elizavet deposits in the Urals. Lithol Mineral Res 36:116–122

440   Tauler E, Proenza J, Galí S, Lewis J, Labrador M, García-Romero E (2009) Ni-sepiolite-falcondite in
441   garnierite mineralisation from the Falcondo Ni-laterite deposit, Dominican Republic. Clay
442   Miner 44: 435–454

443   TOPAS (2009) General profile and structure analysis for powder diffraction data, version 4.2. Bruker
444   AXS, GmbH, Karlsruhe

445   USGS (2015) Mineral commodity summaries 2015. Available at:
446   http://minerals.usgs.gov/minerals/pubs/commodity/platinum/mcs- 2015-plati.pdf. Accessed
447   19.01.2016

448   Varajão CAC, Colin F, Vieillard P, Melfi AJ, Nahon D (2000) Early weathering of palladium gold
449   under lateritic conditions, Maquiné mine, Minas Gerais, Brazil. Appl Geochem 15:245–263

450   Villanova-de-Benavent C, Proenza JA, Galí S, García-Casco A, Tauler E, Lewis JF, Longo F (2014)
451   Garnierites and garnierites: textures, mineralogy and geochemistry of garnierites in the Falcondo
452   Ni-laterite deposit, Dominican Republic. Ore Geol Rev 58:91–109

453   Williams K (1960) An association of awaruite with heazlewoodite. Am Mineral 45:450–453

454   Zaccarini F, Proenza JA, Rudashevsky NS, Cabri LJ, Garuti G, Rudashevsky VN, Melgarejo JC, Lewis
455   JF, Longo F, Bakker RJ, Stanley CJ (2009) The Loma Peguera ophiolitic chromitite
456   (CentralDominican Republic): a source of new platinum group minerals (PGM) species. N Jb
457   Miner Abh 185(3):335–349

458   Zeise WC (1831) I.Von der Wirkung zwischen Platinchlorid und Alkohol, und den dabei entstehenden
459   neuen Substanzen. II. Gekohlenwasserstofftes Chlorplatin-Ammoniak. Annalen der Physik und
460   Chemie (Poggendorff) 21:497–549

461   Zhmodik SM, Shevedenkov GY, Verkhovtseva NV (2004) Iridium distribution in hydrothermally
462   synthesized Fe, Cu, Zn, and Pb sulphides. Can Mineral 42:405–4010

463

Legends to figures

Figure. 1. a The location of the Loma Caribe peridotite and orthophotograph of the Falcondo mining area highlighting the Loma Larga and Loma Peguera ore deposits. b Simplified geological map of the central section of the Loma Caribe peridotite (modified from Bowin 1966; Escuder-Viruete et al. 2007)

Figure. 2 Idealized Ni-laterite soil profile from the Falcondo mining area and field observations of PGE-rich chromitites within saprolite (beneath the Mg discontinuity) and limonite (above the Mg discontinuity)

Figure. 3 Comparison of chondrite normalized PGE patterns of chromitites included in saprolite and limonite showing a clear positive Pt anomaly for the chromitite included in limonite. Normalization values from Naldrett and Duke (1980)

Figure. 4 Secondary electron image of a multistage PGE grain with three characteristic stages of formation (from early to late): (i) Ru- and Os-rich, (ii) Ir-rich, and (iii) Pt-rich.

Figure. 5 EMP analytical profile of relevant elements through the multistage PGE grain of Fig. 4. Note the positive correlation of Fe and Pt through the formation sequence. The neoformed Pt-rich layer appears dark in the reflected light microphotograph at the bottom of the figure.

Figure. 6 Element distribution maps of the multistage PGE grain of Fig. 4. Note the zonation of Ru, Os, Fe and Ir in the lower part of the grain, the visual correlation of Fe and Ni with Pt and Ir enrichment towards the top as well as micron-sized Ru phases at the boundary between Ir-Fe-Ni-(Pt) and Pt-(Ir) sequences

Figure. 7 a Microphotograph of a well-preserved multistage PGE grain obtained by reflected light microscopy showing Os-Ru-rich alloy with a purple appearance, a white band of Ir-rich alloy and white spots of Pt- and Ir-rich nanoparticle accumulations within a reddish matrix of secondary Fe-oxide(s). Note that the microprobe electron beam has left brownish marks on the grain surface. b BSE image of the same grain. c FE-SEM BSE close-up image showing Os-Ru-Fe alloy, Ir-rich layer and Pt-Ir-Fe-Ni nanoparticles. Note that Pt-Ir-Fe-Ni nanoparticles are accumulating around pores (black) within secondary Fe-oxide(s) indicating a close relationship between fluid infill and in situ PGM crystallization

Figure. 8 Element distribution maps of the multistage PGE grain of Fig. 7. Note the advanced stage of supergene Pt incorporation into the secondary PGM (replacement of hypogene PGM by supergene PGM)

Figure. 9 a BSE microphotograph of an unpolished multistage PGE grain showing complete covering of Pt-Ir-Fe-Ni nanoparticles. b FE-SEM BSE close - up image revealing micro- and nanochannels closely linked to Pt-Ir-Fe-Ni nanoparticles. c BSE microphotograph of the same, but polished multistage PGE grain (a) containing a remnant of secondary Ru-Os-Fe alloy with porous appearance in its central part. d FE-SEM BSE close – up image showing the central part of the grain with surrounding Pt-Ir-Fe-Ni nanoparticles within secondary Fe-oxide(s)

Figure. 10 a–h FE-SEM BSE images of characteristic grains of supergene Pt-Ir-Fe-Ni formed by agglutination of nanoparticles. i FE-SEM secondary electron image of one unpolished supergene Pt-Ir-Fe-Ni grain

Figure. 11 Ternary diagrams showing chemical variations for supergene Pt-Ir-Fe-Ni grains. a In the system Ir-Ni-Fe, the data plots suggest Ir and Fe incorporation in awaruite (solid solution). b In the system Pt-Ni-Fe, the data plots suggest Pt incorporation at approx. 60 at.% Fe whereas no correlation with awaruite is observed. c In the system (Pt + Ir)-Ni-Fe a

preference for a composition close to $(Pt, Ir)_{0.3}Ni_{0.25}Fe_{0.45}$ is noted

Figure. 12 Inverse correlation of Ni + Fe vs. Pt + Ir suggesting a solid solution for supergene Pt-Ir-Fe-Ni grains with awaruite
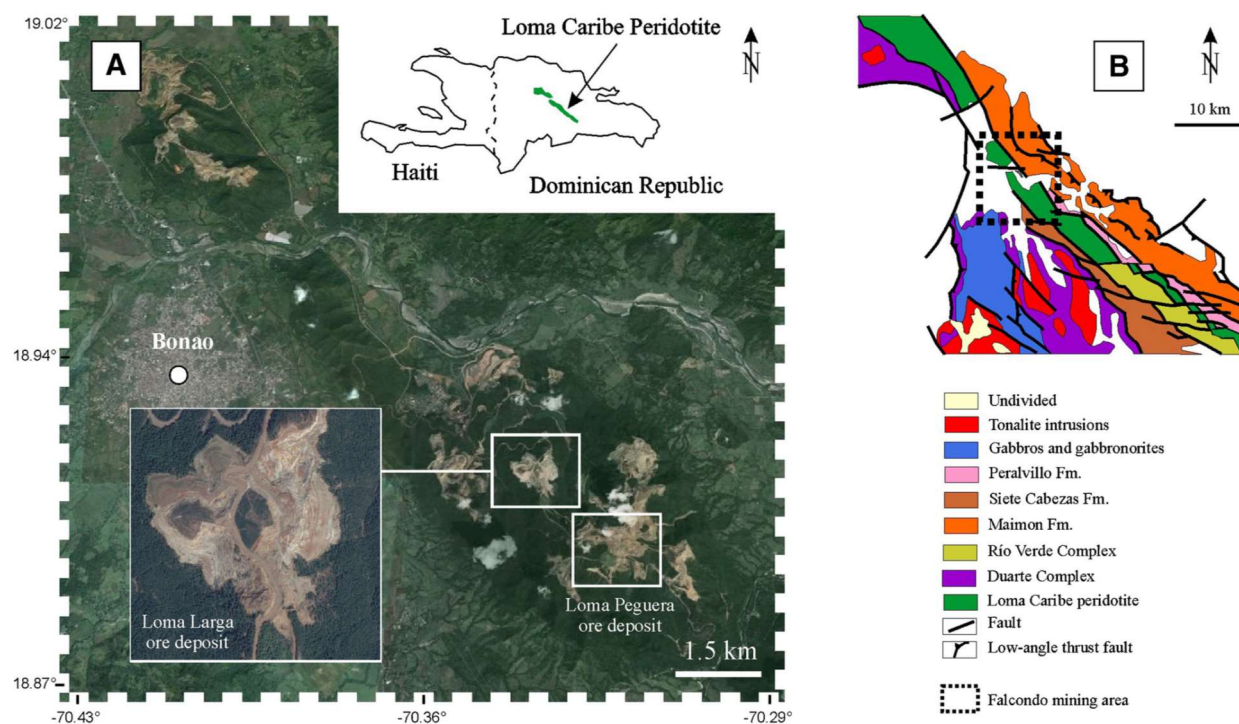
Figure. 13 Observations of the Pt-Ir-Fe-Ni grain selected for XRD analyses. a Stereomicroscope image of the unpolished grain showing metallic luster. b FE-SEM BSE image of the unpolished grain. c FE-SEM BSE close-up image showing accumulations of Pt-Ir-Fe-Ni nanoparticles d FE-SEM BSE image of the polished grain. e FE-SEM BSE close-up image showing densely packed accumulations of Pt-Ir-Fe-Ni nanoparticles. f FE-SEM BSE close-up image showing the growing front with characteristic nano- and microchannels

Figure. 14 Rietveld refinement of the obtained one dimensional conventional diffractogram (TOPAS) and resulting XRD pattern for the Pt-Ir-Fe-Ni alloy. Black observed; red total calculated profile (including background); blue calculated profile for the crystalline phase; grey difference between observed and calculated. Insert shows Debye rings for the Pt-Ir-Fe-Ni alloy, observed on the two-dimensional detector

535   **Figure. 15** A genetic model for the formation of multistage PGE grains: Top row of images (denoted by

536   capital letters) shows idealized cartoons, whereas bottom row of images (denoted by lower case letters)

537   shows examples of actual PGM in the size range of 10-50 μm. A, a Primary PGM included in chromian

538   spinel. B, b Serpentinization and subsequent formation of secondary Ru-Os alloys (bright) with a porous

539   appearance intergrown with Mg silicates (dark). C, c Grain liberation during serpentinization and/or

540   within the saprolite and subsequent formation of Ir-rich Fe-Ni alloys around secondary, highly porous

541   Ru-Os-Fe alloys; D, d Neoformation of Pt-Ir-Fe-Ni nanoparticles in situ within limonite close to the

542   surface around and within secondary Ru-Os-Fe alloys and layers of Ir-Fe-Ni alloys ('growing of PGE

543   nugget')

544

545   **Figure. 16** BSE image of a larger Pt-Ir-Fe-Ni grain (approximately 50×30 μm in diameter). General

546   porosity reduction (e.g. upper right part of the grain) due to particle agglutination
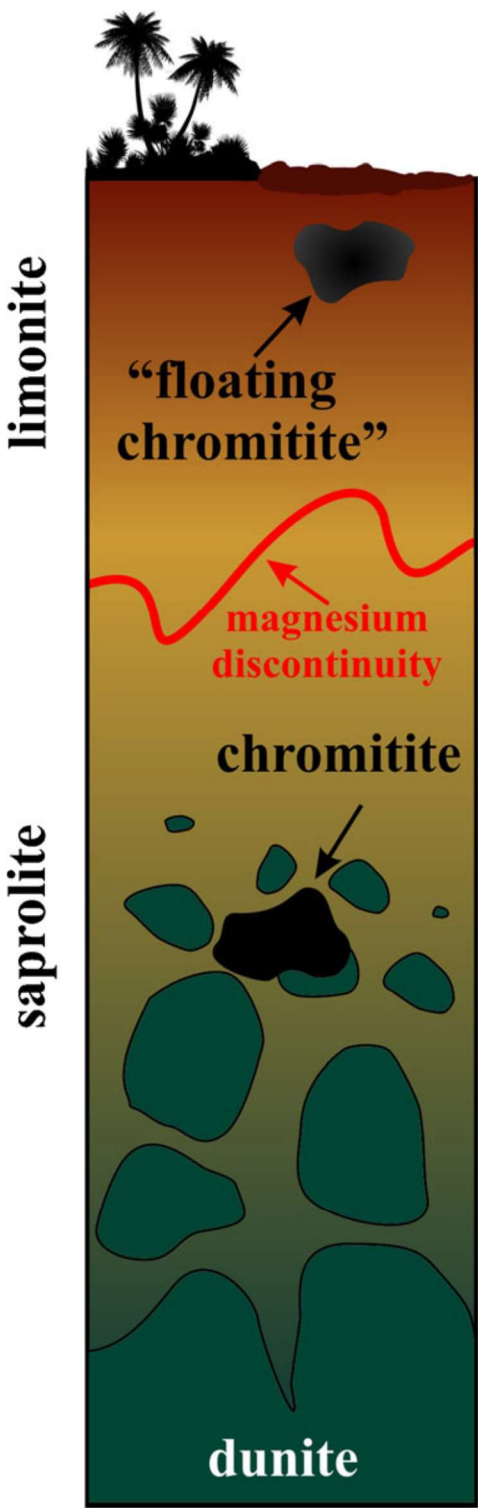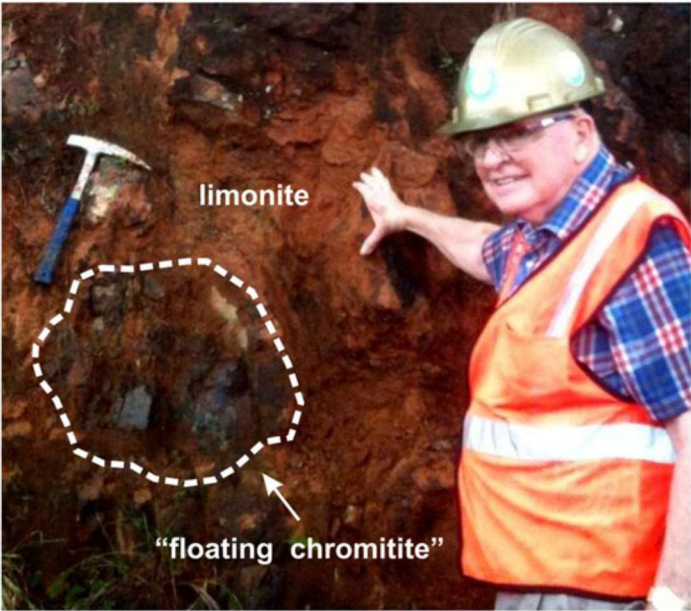
547

FIGURE 1

554   **FIGURE 2**

555

556

FIGURE 3

564 **FIGURE 4**

565

566

567

568

569

FIGURE 5.

571
572
573
574
575
576
577
578
579
580
581
582
583
584
585
586
587
588
589
590
591
592
593

594   **FIGURE 6.**

595

596

597

598

599   **FIGURE 7.**

600

601

602

603

604
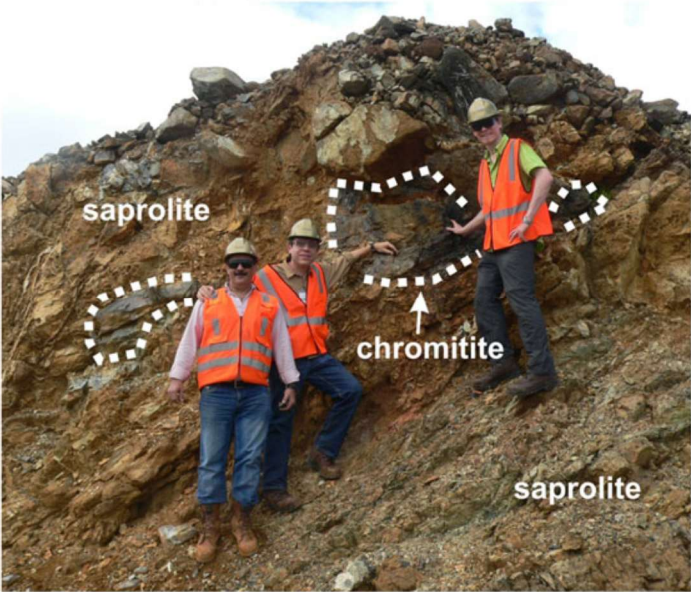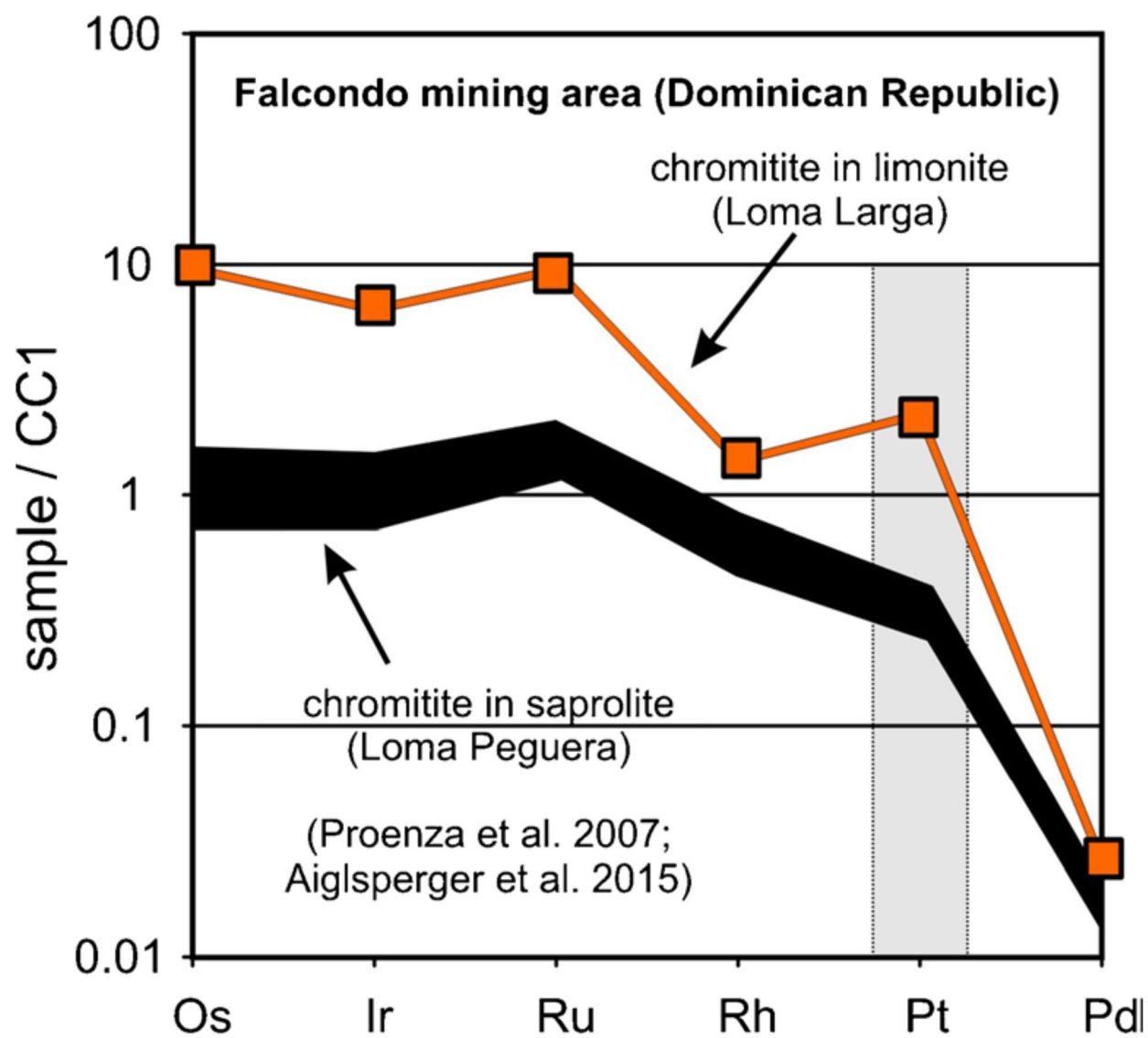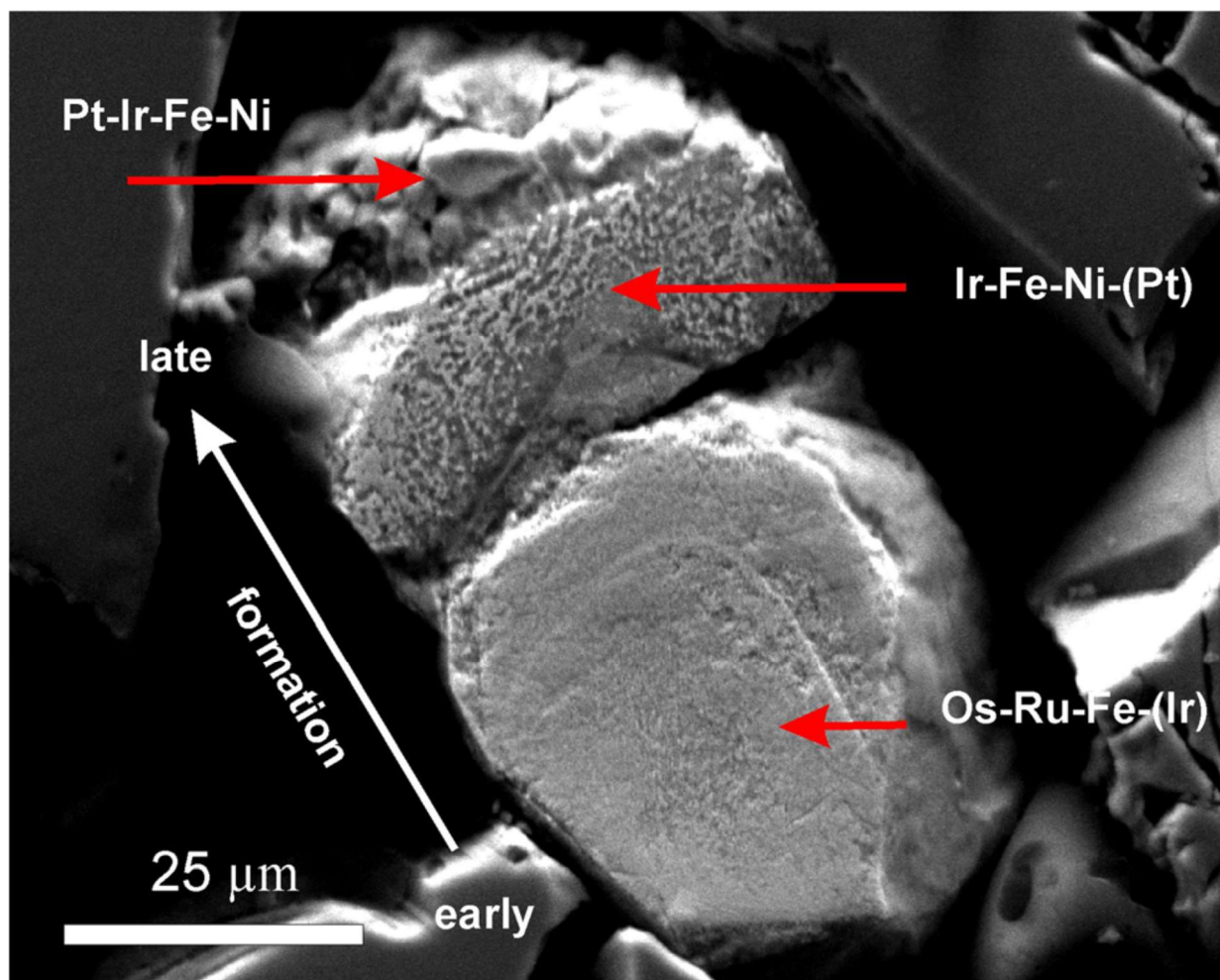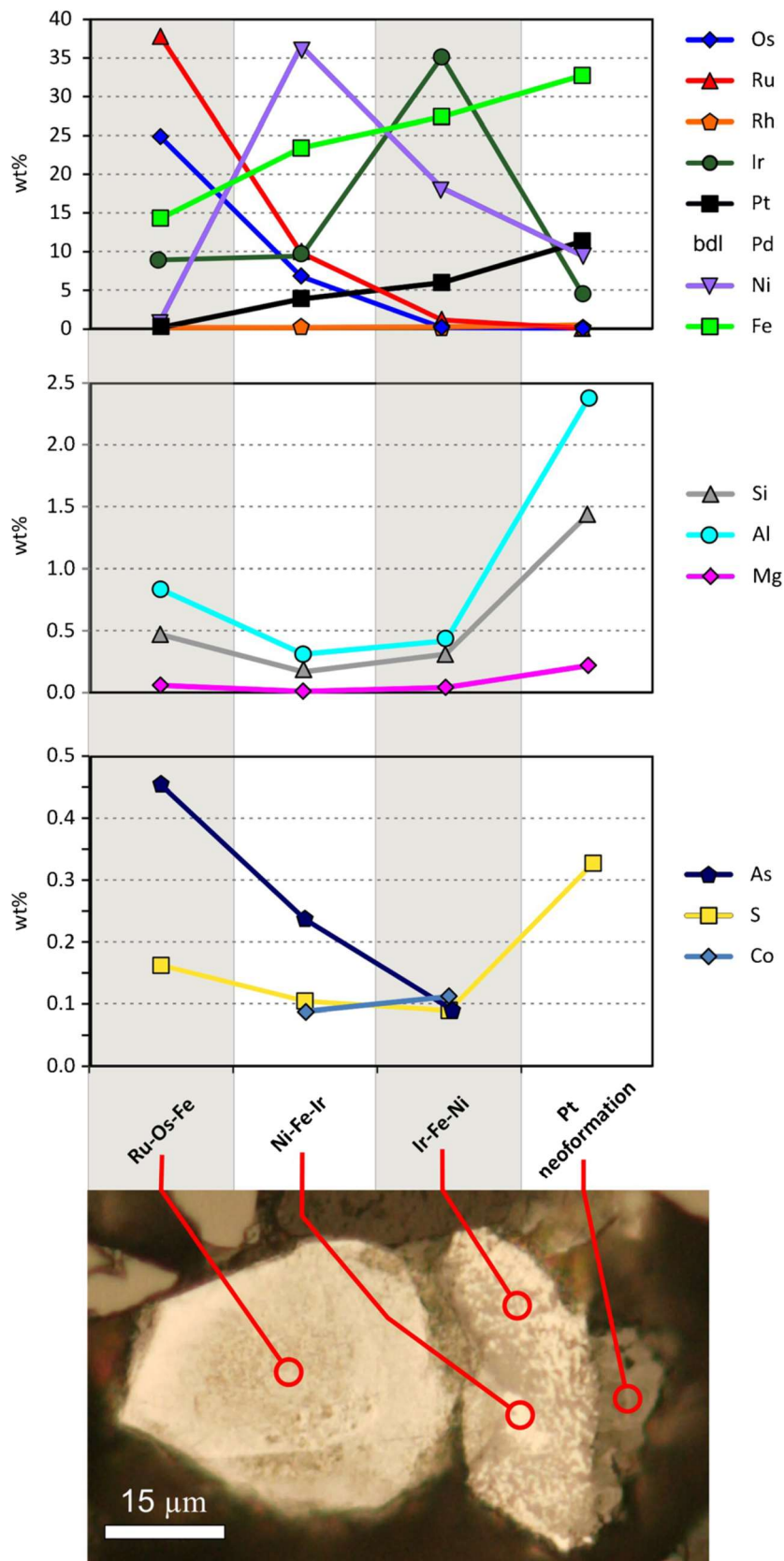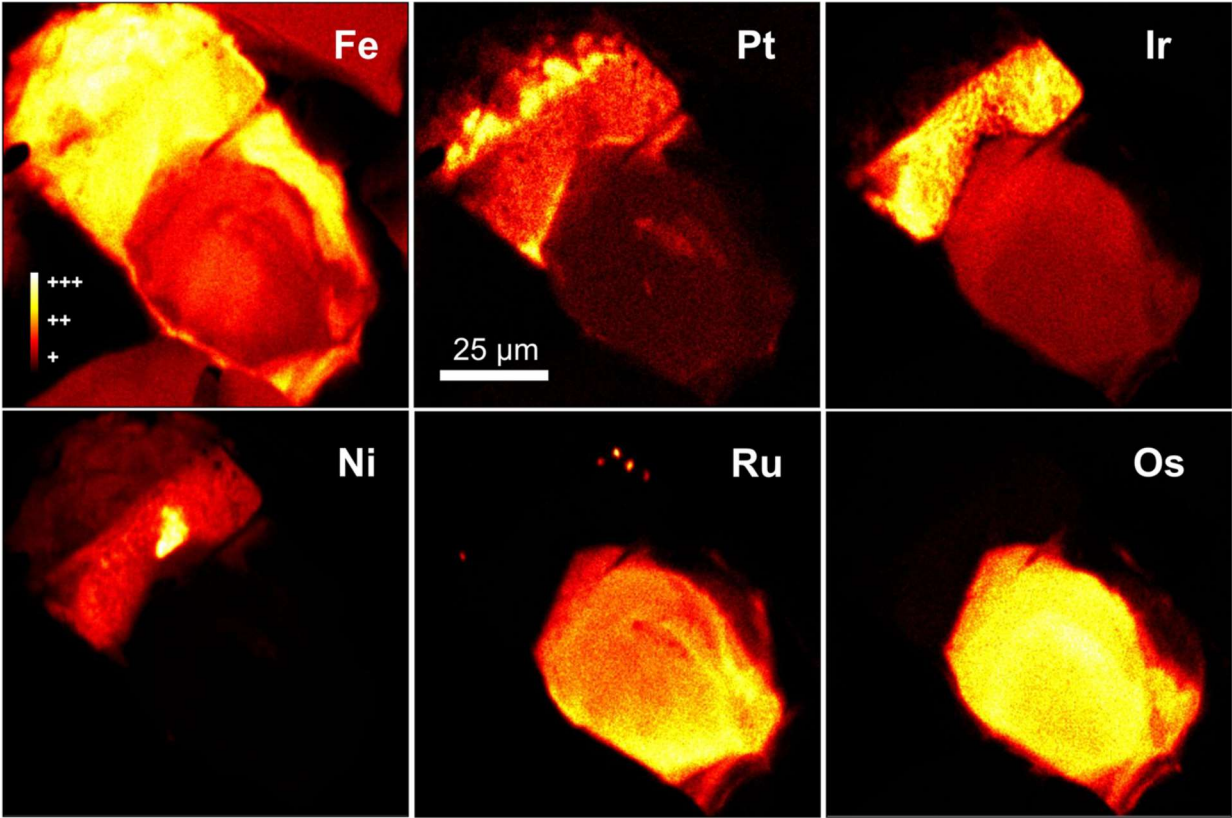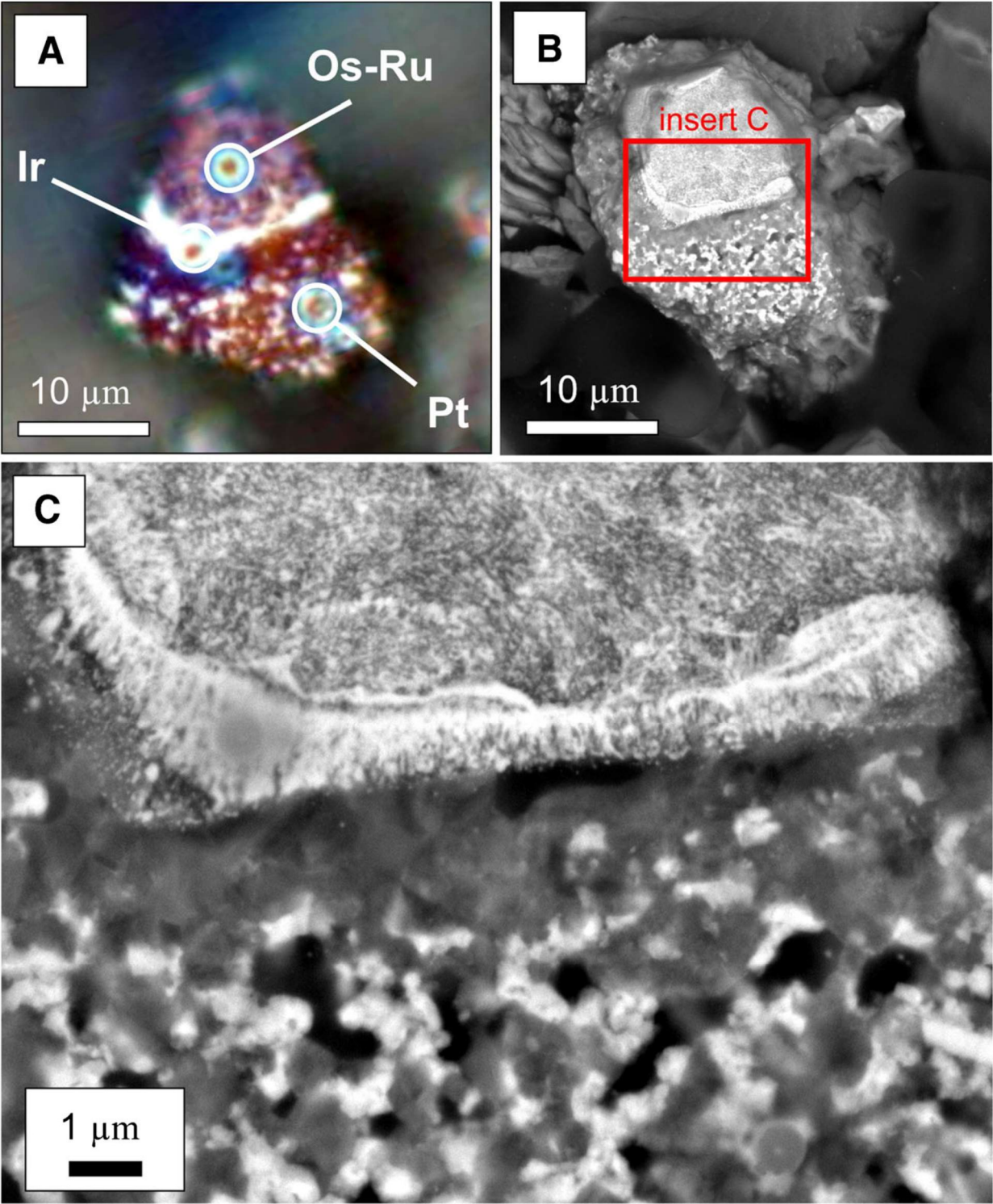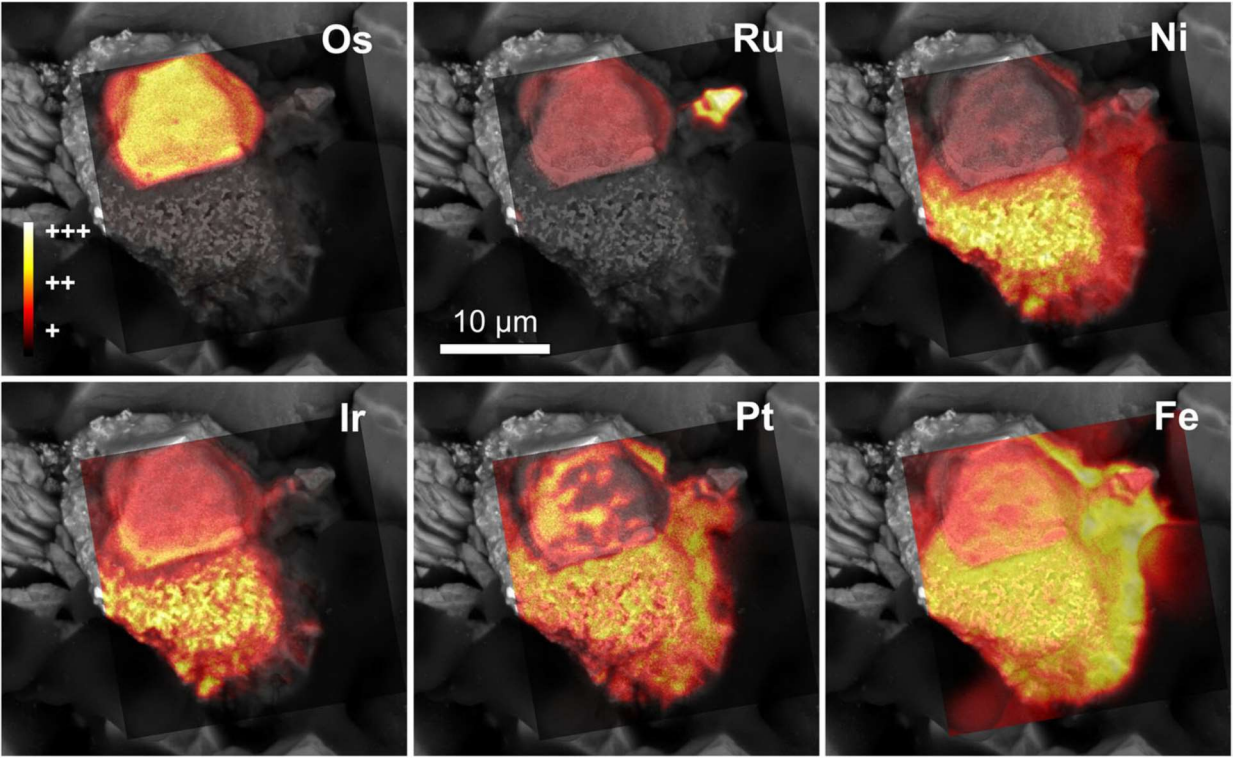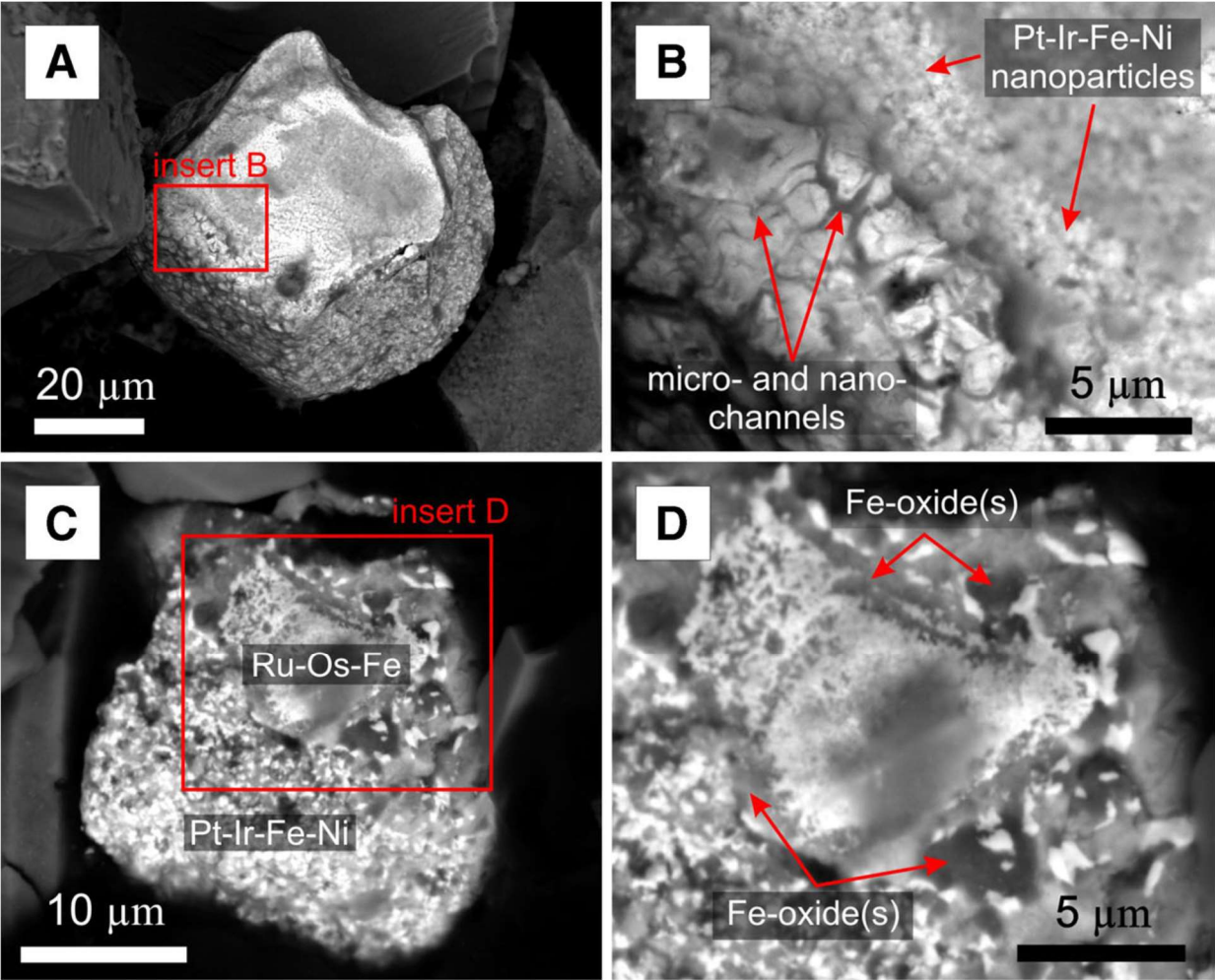
FIGURE 8.

FIGURE 9.

615   **FIGURE 10.**

616

617

618

619

FIGURE 11.

622
623
624
625
626
627
628
629
630
631
632
633
634
635
636
637
638
639
640
641
642
643
644
645
646
647
648
649
650
651
652
653
654
655
656
657
658
659
660
661
662
663
664
665
666
667
668

FIGURE 12.

669
670
671

672
673
674
675

FIGURE 13.

679
680
681
682
683
684

FIGURE 14.

$(Pt,Ir)_{0.28}Ni_{0.27}Fe_{0.45}$

FIGURE 15.

STAGES OF PGM (TRANS-)FORMATION

FIGURE 16.

Pt-Ir-Fe-Ni

15 μm
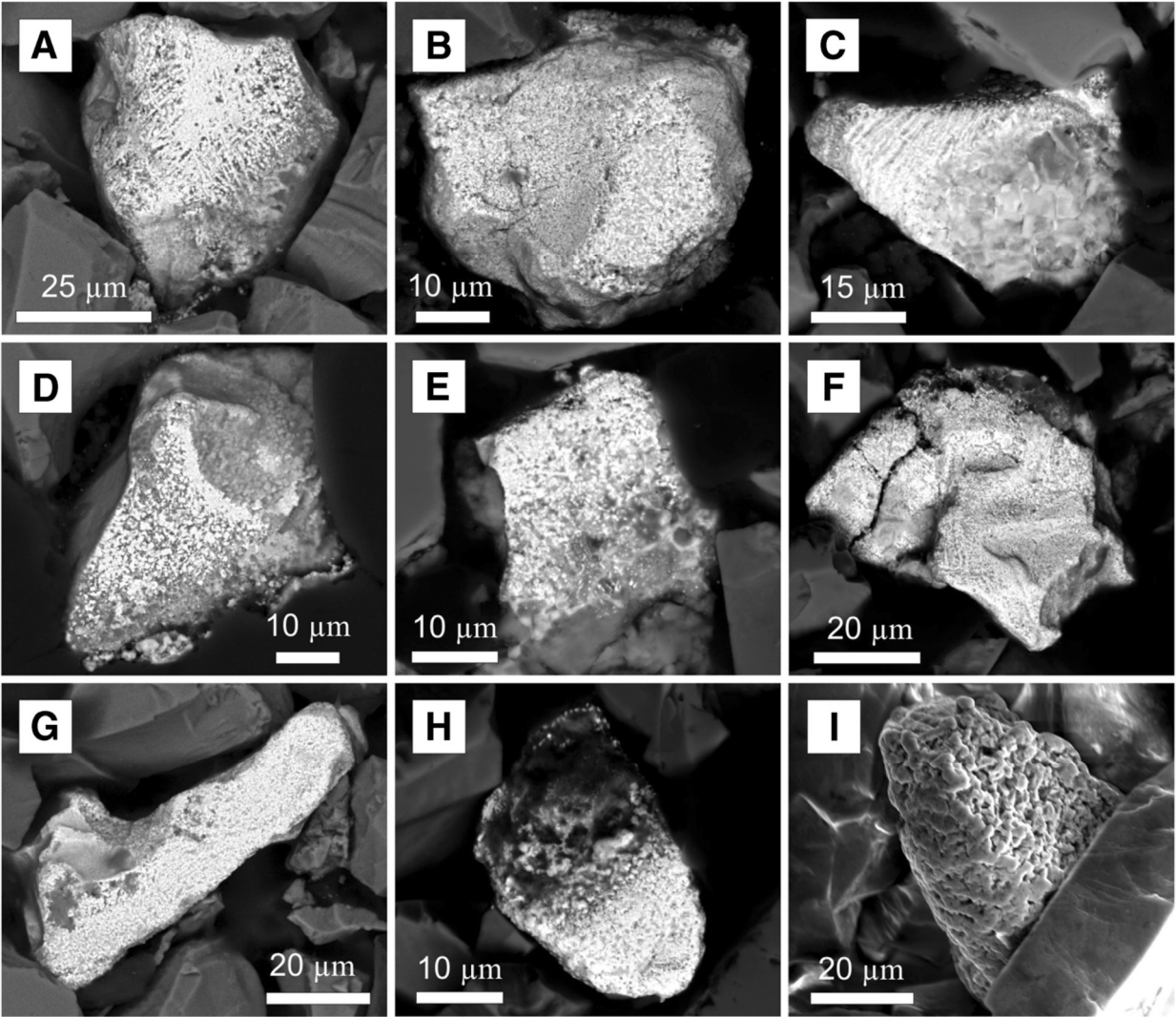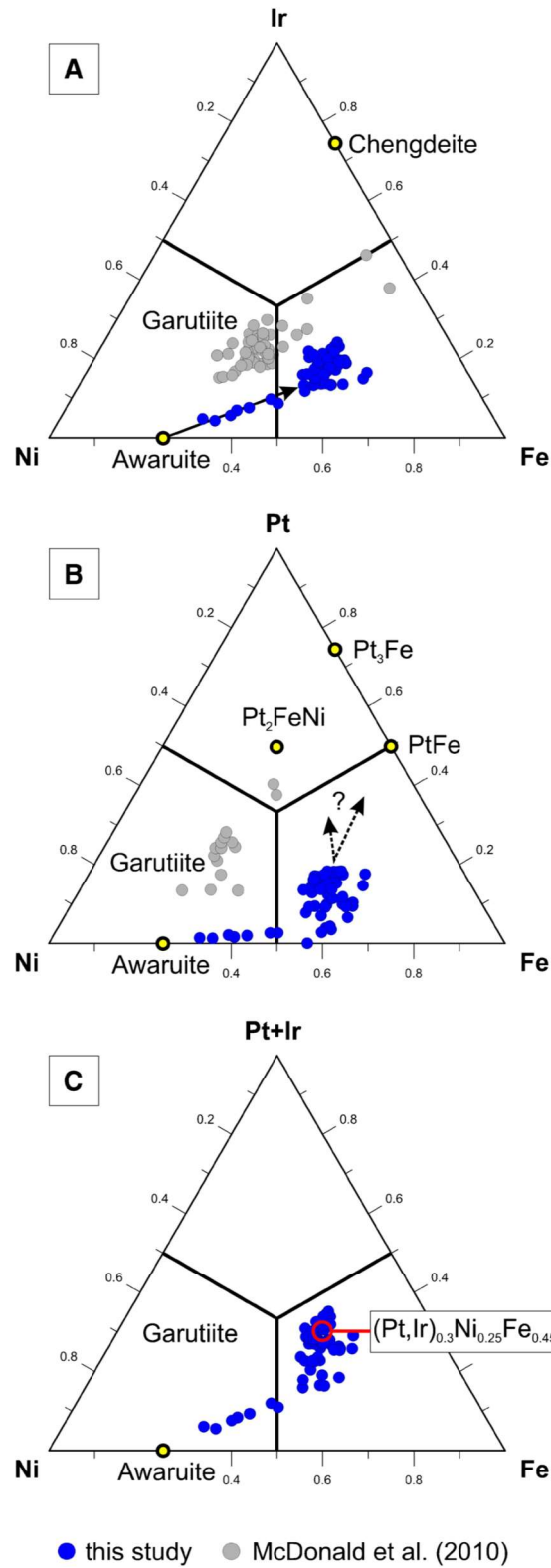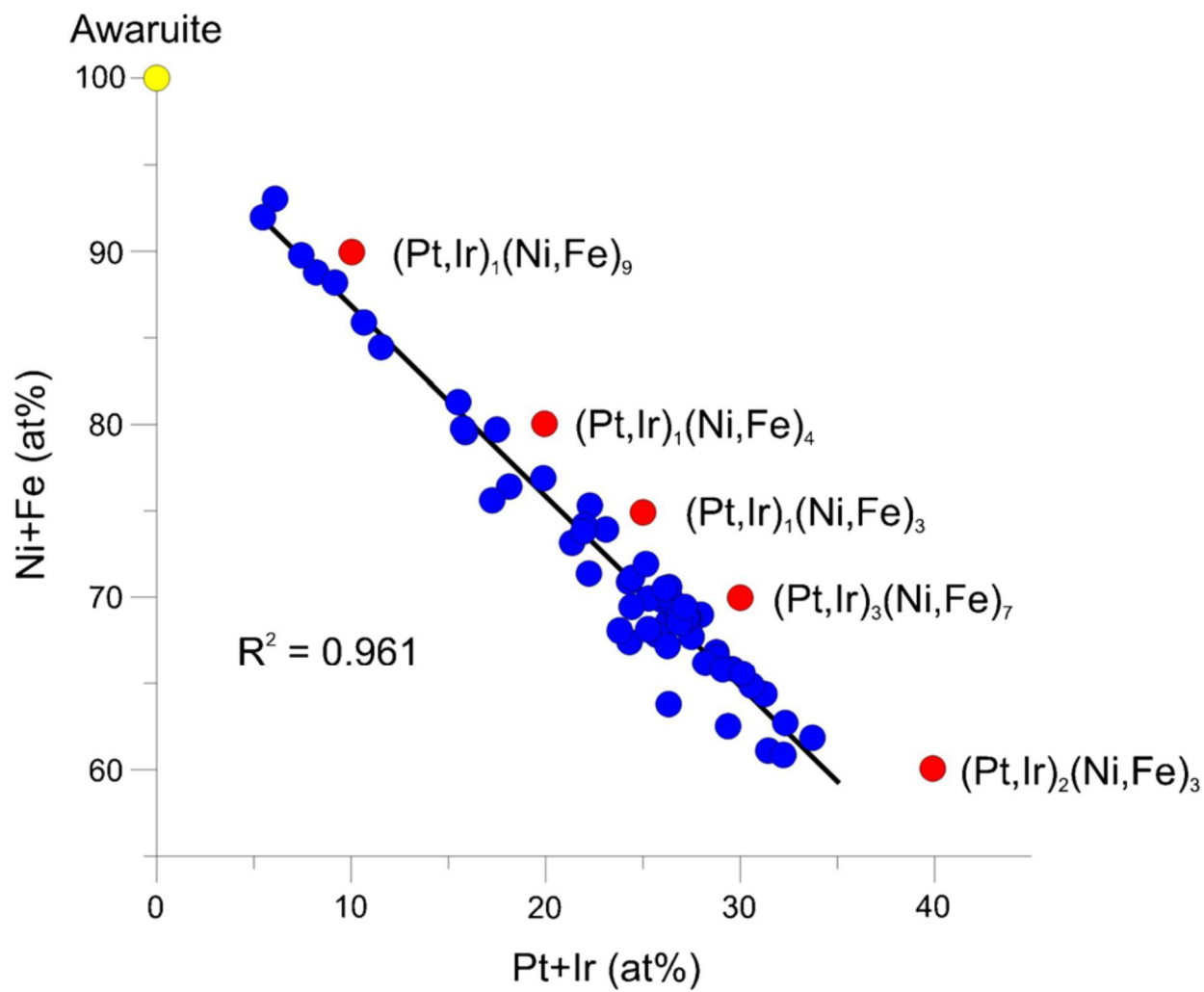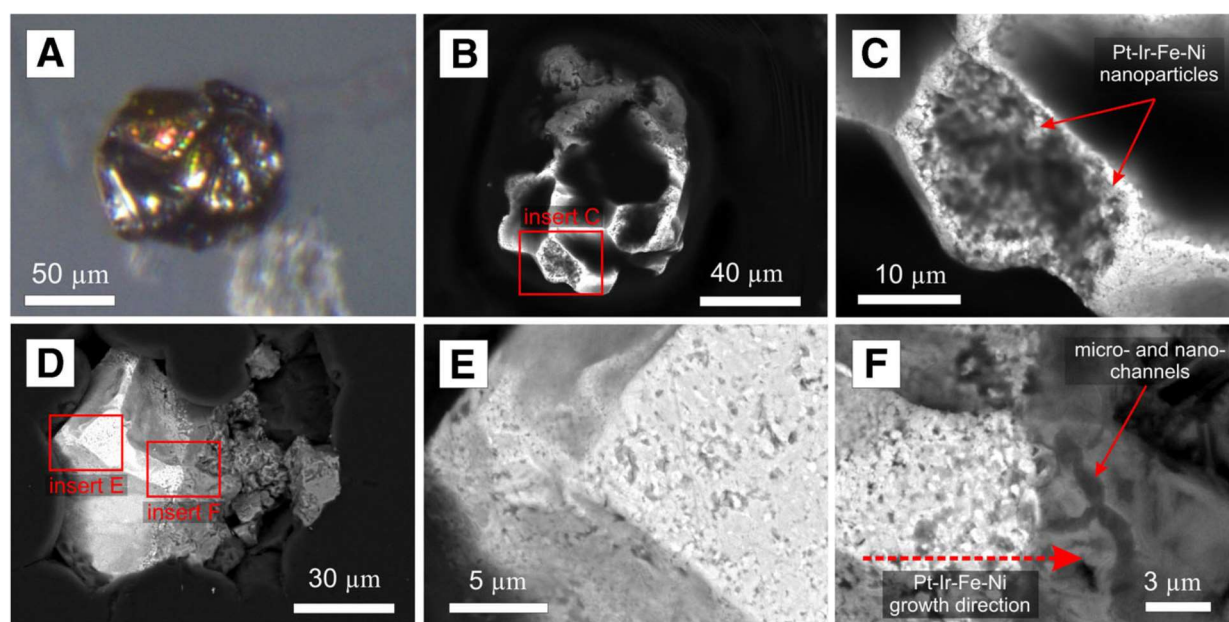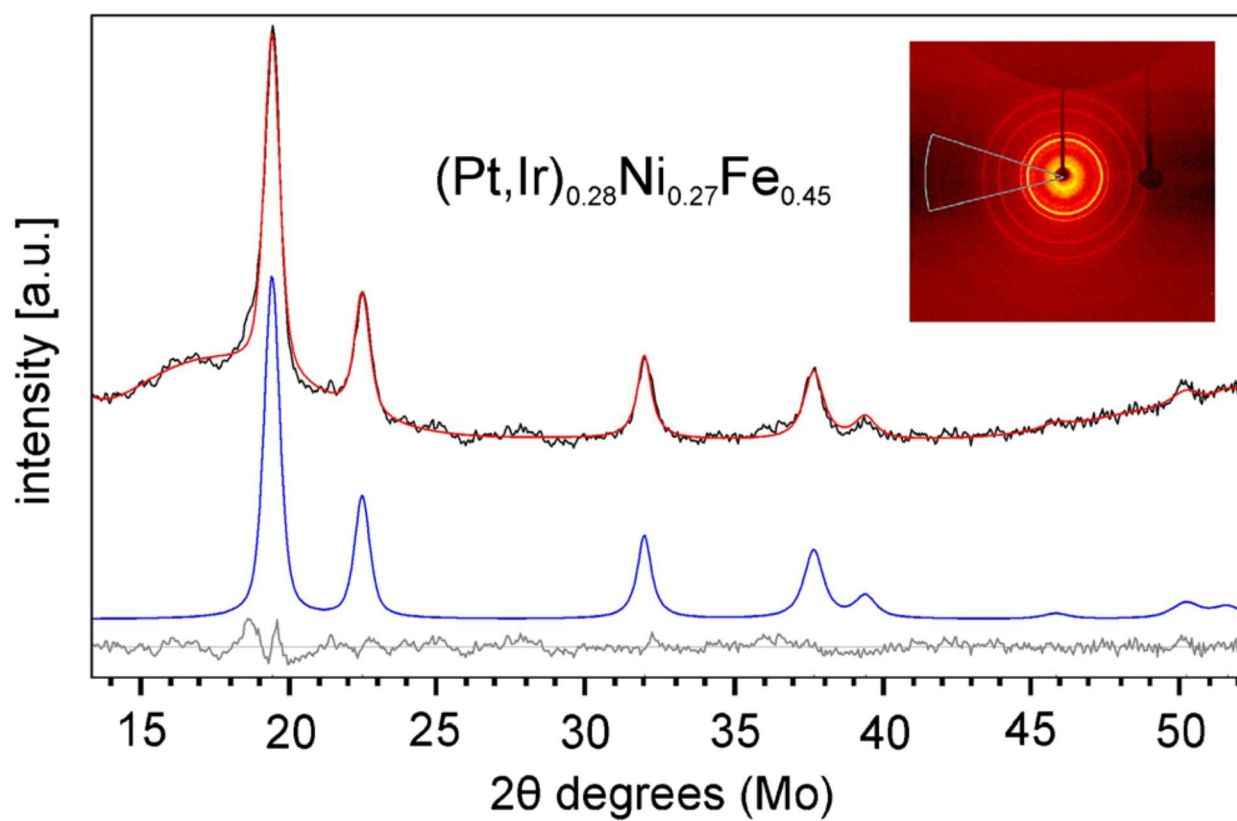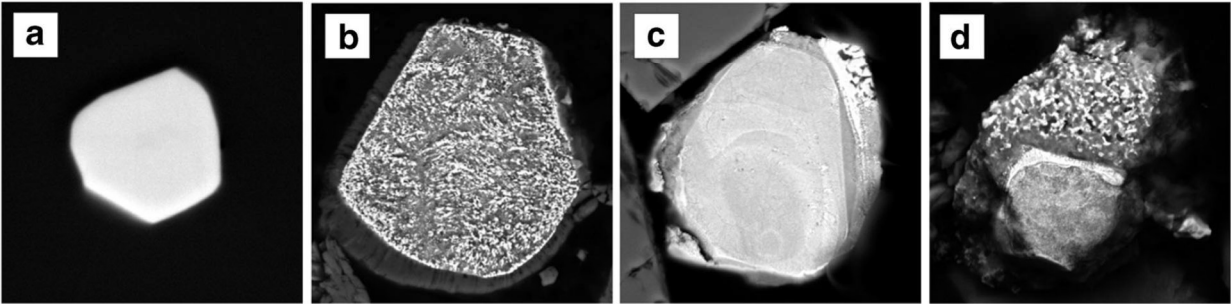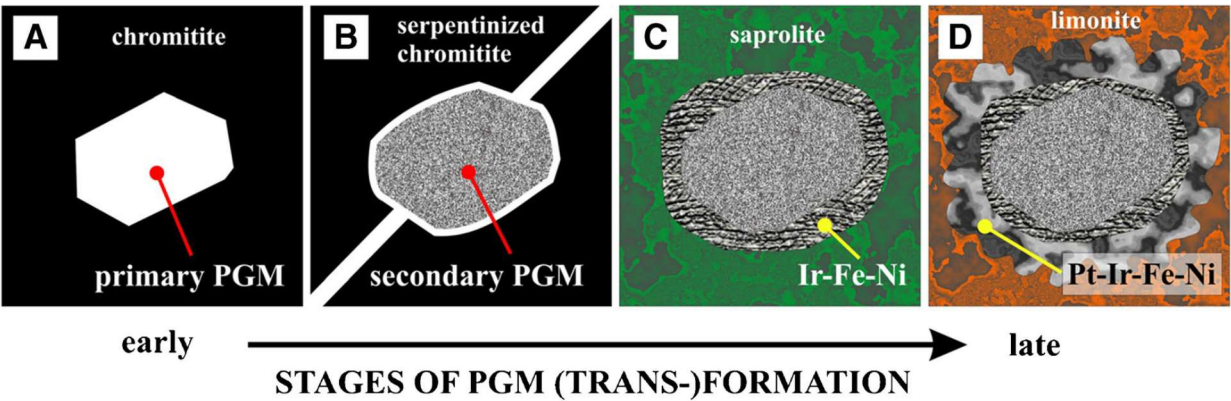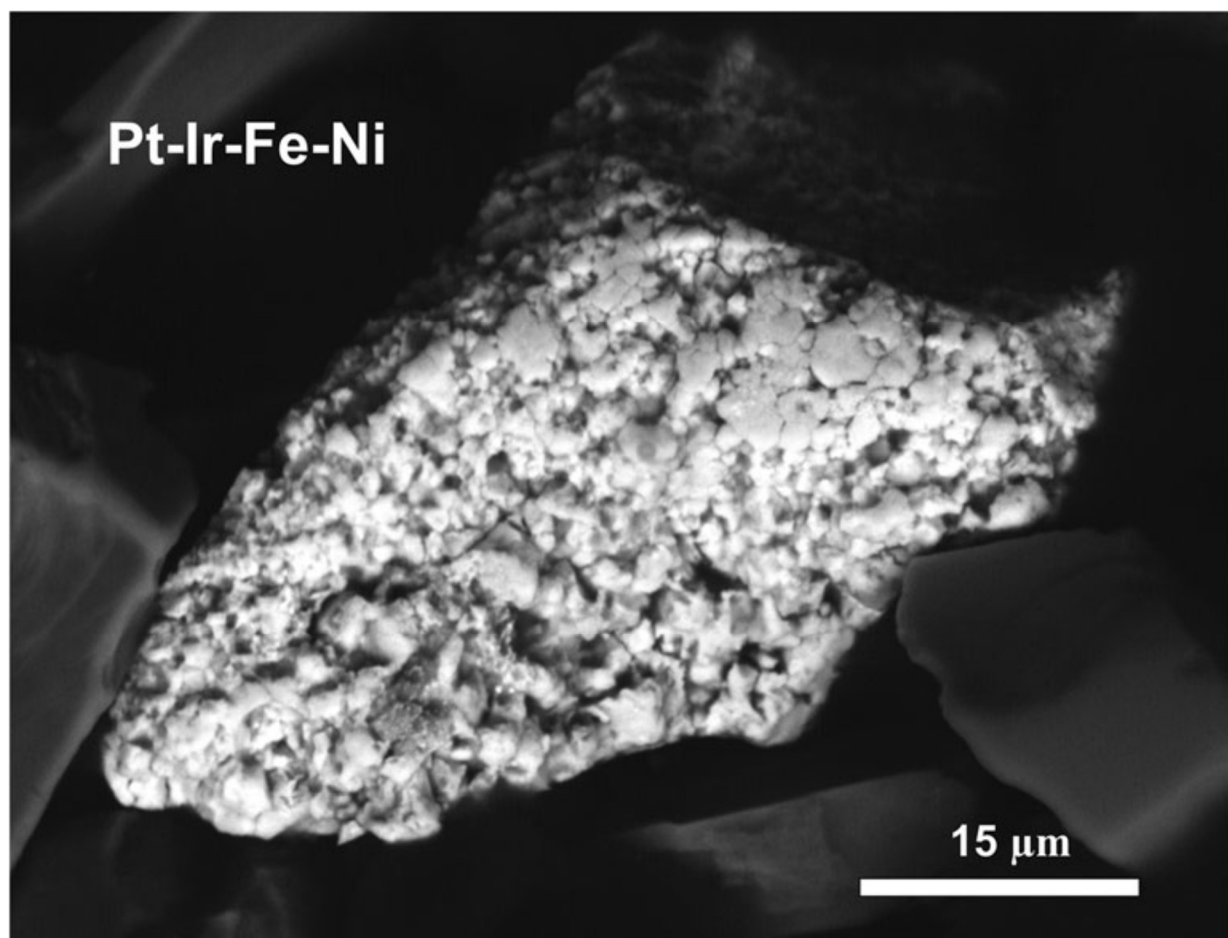
707   **Table 1** Comparison of the whole rock PGE geochemistry of chromitite included in saprolite from

708   Loma Peguera (Aiglsperger et al. 2015) and chromitite included in limonite from Loma Larga (this

709   study)

[ppb]	Loma Peguera Chromitite Saprolite	Loma Larga Chromitite Limonite
Os	812	4945
Ir	802	3455
Ru	1396	6536
Rh	152	281
Pt	408	2282
Pd	8	14
PGE	3578	17,513
Pt/Pd	51	163
Pt/Ir	0.51	0.66
Pt/Rh	2.68	8.12
Pt/Ru	0.29	0.35
Pt/Os	0.50	0.46
IPGE	3010	14,936
PPGE	568	2577
IPGE/PPGE	5.3	5.8

710

711

712   **Table 2** EMP analyses of the analysed points displayed in Fig. 5. The low totals result from the fine-
713   grained nature of grains and/or high porosities of surfaces
714

[wt%]	Ru-Os-Fe	Ni-Fe-Ir	Ir-Fe-Ni	Pt neoformation
Os	24.83	6.81	0.19	0.07
Ru	37.75	9.87	1.17	0.10
Ir	8.94	9.44	35.14	4.62
Rh	0.20	0.18	0.26	0.50
Pt	0.20	3.90	5.99	11.34
Pd	bdl	bdl	bdl	bdl
S	0.16	0.10	0.09	0.33
As	0.45	0.24	0.09	bdl
Fe	14.32	23.39	27.42	32.74
Ni	1.20	36.54	18.25	9.50
Co	bdl	0.09	0.11	bdl
Sb	bdl	bdl	bdl	bdl
Mg	0.06	0.01	0.04	0.22
Si	0.47	0.17	0.31	1.44
Al	0.83	0.31	0.42	2.37
Total	89.41	91.04	89.48	63.21

715
716

Table 3　Selected results of EMP analyses of characteristic Pt-Ir-Fe-Ni alloys

Composition of nonformed Pt-Ir-Fe-Ni alloys analysed by Electron Microprobe

wt%

	S	As	Os	Ir	Ru	Rh	Pt	Pd	Fe	Ni	Cu	Co	Si	Al	Mg	Sb	Total
LL_PGM1_2	0.03	0.09	0.13	31.12	1.81	1.58	11.26	bdl	25.41	17.44	n.a.	0.16	0.29	0.19	0.01	0.02	89.53
LL_PGM3_1	0.03	bdl	0.23	32.26	0.26	1.80	19.66	bdl	19.68	14.41	n.a.	0.07	0.33	0.14	bdl	bdl	88.86
LL_PGM4_1	0.09	bdl	bdl	28.33	0.06	0.30	22.82	bdl	19.09	11.90	n.a.	0.05	0.57	0.22	0.03	bdl	83.45
LL_PGM4_2	0.02	bdl	0.13	30.00	0.06	0.30	20.70	bdl	22.58	15.04	n.a.	0.08	0.53	0.30	0.04	bdl	89.77
LL_PGM4_5	0.02	bdl	bdl	29.04	0.08	0.33	15.84	bdl	25.39	19.41	n.a.	0.08	0.30	0.22	bdl	bdl	90.71
LL_PGM5_4	0.02	0.06	0.16	32.80	0.20	1.34	17.34	bdl	24.38	14.47	n.a.	0.28	0.27	0.13	0.02	bdl	91.48
LL_PGM6_2	bdl	bdl	bdl	32.63	0.24	1.56	14.37	0.03	26.43	13.80	n.a.	0.32	0.32	0.22	0.03	bdl	89.94
LL_PGM7_1	0.01	0.08	0.54	13.06	0.16	0.18	3.81	bdl	24.48	52.71	n.a.	0.13	0.06	0.02	bdl	bdl	95.22
LL_PGM7_2	0.04	0.16	0.20	40.12	1.57	0.28	4.55	0.04	26.28	18.30	0.45	0.13	0.21	0.17	0.04	bdl	92.08
LL_PGM9_1	bdl	0.13	0.43	34.11	1.76	0.14	bdl	0.10	29.61	23.74	0.76	0.14	0.07	bdl	bdl	0.10	90.77
LL_PGM11_1	bdl	bdl	bdl	30.57	0.02	0.41	21.97	0.06	18.77	9.52	1.30	0.09	0.27	0.17	0.02	bdl	82.63
LL_PGM12_3	0.05	bdl	bdl	14.27	0.33	0.38	5.38	bdl	26.87	43.92	0.83	0.27	0.08	bdl	bdl	bdl	92.85
LL_PGM14_1	bdl	bdl	bdl	23.85	0.10	0.59	23.90	bdl	28.45	11.48	0.43	0.26	0.07	bdl	bdl	bdl	89.53
LL_PGM15_2	0.01	0.08	bdl	19.68	0.14	1.26	5.93	0.25	30.02	31.26	0.49	0.72	0.10	0.08	bdl	bdl	89.96
LL_PGM15_3	0.03	0.10	0.47	11.51	0.09	0.79	3.48	bdl	26.07	49.37	1.30	0.68	0.07	bdl	0.04	bdl	93.14
Max.	0.09	0.16	0.54	40.12	1.81	1.80	23.90	0.25	30.02	52.71	1.30	0.72	0.57	0.30	0.04	0.10	95.22
Min.	bdl	bdl	bdl	11.51	0.02	0.14	bdl	bdl	18.77	9.52	0.43	0.05	0.06	bdl	bdl	bdl	82.63
Avg.	0.02	0.05	0.15	26.89	0.46	0.75	12.73	0.03	24.90	23.12	0.71	0.23	0.24	0.12	0.01	0.01	90.00

at%

	S	As	Os	Ir	Ru	Rh	Pt	Pd	Fe	Ni	Cu	Co	Si	Al	Mg	Sb
LL_PGM1_2	0.08	0.12	0.07	15.74	1.74	1.49	5.61	0.00	44.25	28.90	n.a.	0.26	0.99	0.69	0.05	0.01
LL_PGM3_1	0.09	0.00	0.13	18.49	0.29	1.93	11.10	0.00	38.82	27.04	n.a.	0.12	1.30	0.58	0.00	0.00
LL_PGM4_1	0.33	0.00	0.00	17.42	0.07	0.34	13.83	0.00	40.41	23.97	n.a.	0.09	2.39	0.98	0.12	0.00
LL_PGM4_2	0.06	0.00	0.07	16.25	0.06	0.30	11.05	0.00	42.10	26.68	n.a.	0.14	1.97	1.17	0.16	0.00
LL_PGM4_5	0.07	0.09	0.00	14.49	0.08	0.31	7.79	0.00	43.59	31.71	n.a.	0.13	1.02	0.79	0.00	0.00
LL_PGM5_4	0.05	0.00	0.09	17.41	0.20	1.33	9.07	0.02	44.54	25.15	n.a.	0.49	0.97	0.51	0.10	0.00
LL_PGM6_2	0.00	0.00	0.00	17.04	0.24	1.52	7.40	0.02	47.52	23.61	n.a.	0.54	1.14	0.82	0.11	0.00
LL_PGM7_1	0.03	0.07	0.20	4.73	0.11	0.12	1.36	0.00	30.52	62.52	n.a.	0.15	0.14	0.04	0.00	0.00
LL_PGM7_2	0.11	0.21	0.10	19.79	1.47	0.26	2.21	0.04	44.61	29.56	0.61	0.20	0.71	0.58	0.16	0.07
LL_PGM9_1	0.00	0.15	0.20	15.43	1.51	0.12	0.00	0.08	46.12	35.18	1.49	0.21	0.21	0.00	0.00	0.00
LL_PGM11_1	0.11	0.00	0.00	19.74	0.02	0.50	13.98	0.07	41.71	20.13	1.49	0.19	1.19	0.78	0.11	0.00
LL_PGM12_3	0.00	0.00	0.00	5.42	0.24	0.27	2.01	0.00	35.13	54.64	1.33	0.33	0.21	0.00	0.00	0.00
LL_PGM14_1	0.11	0.00	0.00	12.66	0.10	0.59	12.50	0.00	51.96	19.95	0.54	0.45	0.26	0.00	0.00	0.00
LL_PGM15_2	0.02	0.08	0.00	8.22	0.11	0.98	2.44	0.19	43.14	42.74	0.54	0.98	0.29	0.25	0.00	0.00
LL_PGM15_3	0.07	0.09	0.17	4.21	0.07	0.54	1.25	0.00	32.83	59.15	1.49	0.81	0.17	0.00	0.00	0.00
Max.	0.33	0.21	0.20	19.79	1.74	1.93	13.98	0.19	51.96	62.52	1.49	0.98	2.39	1.17	0.16	0.07
Min.	0.00	0.00	0.00	4.21	0.02	0.12	0.00	0.00	30.52	19.95	0.54	0.09	0.14	0.00	0.00	0.00
Avg.	0.07	0.05	0.07	13.80	0.42	0.71	6.77	0.03	41.82	34.06	1.00	0.34	0.86	0.48	0.05	0.01

717
718
719
720
721
722
723
724
725
726
727
728

Table 4 Powder x-ray data for the Pt-Ir-Fe-Ni alloy and comparison with chemically related phases

Pt-Ir-Fe-Ni alloy			Awaruite[a]			Isoferroplatinum[b]			Ferronickelplatinum[c]			Garutiite[d]		
$(Pt,Ir)_{0.28}Ni_{0.27}Fe_{0.45}$ Fm3m			PDF 38-419 (Ni_3Fe) Pm3m			PDF 29-1423 (Pt_3Fe) Pm3m			PDF 35-702 Pt_2FeNi P4/mmm			Ni P63/mmc		
Imeas	dmeas(Å)	hkl	Imeas	dmeas(Å)	hkl	Imeas	dmeas(Å)	hkl	Imeas	dmeas(Å)	hkl	Imeas	dmeas(Å)	hkl
									10	3.660	001			
									10	2.752	110			
												50	2.330	100
									100	2.192	100	30	2.136	002
100	2.1017	111	100	2.044	111	60	2.220	111				100	2.046	101
						100	1.934	200	50	1.935	020			
35	1.8202	200	60	1.772	200	20	1.724	210	10	1.830	002			
									30	1.699	021			
									10	1.509	112	30	1.576	102
									10	1.371	220			
									40	1.324	022	40	1.3470	110
									10	1.294	030			
25	1.28704	220	30	1.253	220				10	1.277	221	40	1.2155	103
									10	1.221	130	10	1.1669	200
									30	1.157	013	20	1.1391	112
									20	1.092	222	20	1.1256	201
20	1.0976	311	40	1.069	311	10	1.572	211				5	1.0680	004
10	1.0509	222	10	1.023	222	70	1.364	220				5	1.0239	202
3	0.9101	004										5	0.9715	104
5	0.8351	331	10	0.814	331	100	1.165	311						
4	0.8140	420	10	0.792	420	50	1.114	222						
						10	1.070	320						
						20	1.031	321						

[a] Williams (1960)
[b] Begizov et al. (1975)
[c] Rudashevsky et al. (1983)
[d] McDonald et al. (2010)

735   **Table 5** Comparative data for chemically related alloys including Pt-Ir-Fe-Ni

	Pt-Ir-Fe-Ni	Awaruite[a]	Isoferroplatinum[b]	Ferronickelplatinum[c]	Garutiite[d]
Chemical formula	$(Pt, Ir)_{0.28}Ni_{0.27}Fe_{0.45}$	Ni_3Fe	Pt_3Fe	Pt_2FeNi	(Ni, Fe, Ir)
Crystal System	Cubic	Cubic	Cubic	Tetragonal	Hexagonal
Group:	$Fm3m$	$Pm3m$	$Pm3m$	$P4/mmm$	$P63/mmc$
Unit cell:					
a (Å)	3.6403(17)	3.5450	3.8580	3.8710	2.6939(5)
c (Å)				3.6350	4.2732(6)
V (Å3)	48.240(69)	44.55	57.42	54.47	26.86(1)
Z	4	1	1	1	2

[a] Williams (1960)
[b] Begizov et al. (1975)
[c] Rudashevsky et al. (1983)
[d] McDonald et al. (2010)

736

737